

1 **Technical Note: Constraining the hydroxyl (OH) radical in the tropics with satellite observations of its**  
2 **drivers: First steps toward assessing the feasibility of a global observation strategy**

3  
4 Daniel C. Anderson<sup>1,2</sup>, Bryan N. Duncan<sup>2</sup>, Julie M. Nicely<sup>2,3</sup>, Junhua Liu<sup>2,4</sup>, Sarah A. Strode<sup>2,4</sup>, Melanie B.  
5 Follette-Cook<sup>5</sup>

- 6  
7 1. GESTAR II, University of Maryland Baltimore County, Baltimore, MD, USA  
8 2. Atmospheric Chemistry and Dynamics Laboratory, NASA Goddard Space Flight Center, Greenbelt,  
9 MD, USA  
10 3. Earth System Science Interdisciplinary Center, University of Maryland, College Park, MD, USA  
11 4. GESTAR II, Morgan State University, Baltimore, MD, USA  
12 5. Mesoscale Atmospheric Processes Laboratory, NASA Goddard Space Flight Center, Greenbelt, MD,  
13 USA

14  
15 *Correspondence to:* Daniel C. Anderson (daniel.c.anderson@nasa.gov)

16  
17 **Abstract**

18 Despite its importance in controlling the abundance of methane (CH<sub>4</sub>) and a myriad of other  
19 tropospheric species, the hydroxyl radical (OH) is poorly constrained due to its large spatial  
20 heterogeneity and the inability to measure tropospheric OH with satellites. Here, we present a  
21 methodology to infer tropospheric column OH (TCOH) in the tropics over the open oceans using a  
22 combination of a machine learning model, output from a simulation of the GEOS model, and satellite  
23 observations. Our overall goals are to assess the feasibility of our methodology, to identify potential  
24 limitations, and to suggest areas of improvement in the current observational network. The  
25 methodology reproduces the variability of TCOH from independent 3D model output and of  
26 observations from the Atmospheric Tomography mission (ATom). While the methodology also  
27 reproduces the magnitude of the 3D model validation set, the accuracy of the magnitude when applied  
28 to observations is uncertain because current observations are insufficient to fully evaluate the machine  
29 learning model. Despite large uncertainties in some of the satellite retrievals necessary to infer OH,  
30 particularly for NO<sub>2</sub> and HCHO, current satellite observations are of sufficient quality to apply the  
31 machine learning methodology, resulting in an error comparable to that of *in situ* OH observations.  
32 Finally, the methodology is not limited to a specific suite of satellite retrievals. Comparison of TCOH  
33 determined from two sets of retrievals does show, however, that systematic biases in NO<sub>2</sub>, resulting  
34 both from retrieval algorithm and instrumental differences, lead to relative biases in the calculated  
35 TCOH. Further evaluation of NO<sub>2</sub> retrievals in the remote atmosphere is needed to determine their  
36 accuracy. With slight modifications, a similar methodology could likely be expanded to the extra-tropics  
37 and over land, with the benefits of increasing our understanding of the atmospheric oxidation capacity  
38 and, for instance, informing understanding of recent CH<sub>4</sub> trends.

39  
40 **1 Introduction**

41 The hydroxyl radical (OH) dictates the lifetime of many tropospheric species, including carbon monoxide  
42 (CO), methane (CH<sub>4</sub>), and numerous volatile organic compounds (VOCs). Knowledge of OH is therefore  
43 necessary to understand the abundance, distribution, and variability of these species. For instance,  
44 Rigby et al. (2017) and Laughner et al. (2021) attribute recent trends and increases in CH<sub>4</sub> at least  
45 partially to changes in OH abundance. Current constraints on OH are insufficient, however, to assess its  
46 relative importance in controlling these trends (Turner et al., 2017).

48 Differences in OH distributions among chemistry transport (CTM) and chemistry climate models (CCM)  
49 suggest that these models are insufficient to inform understanding of OH abundance and variability  
50 without further observational constraints. OH abundance can differ by up to 80% among models  
51 constrained with identical emissions in intercomparison projects (Voulgarakis et al., 2013; Nicely et  
52 al.; Zhao et al., 2019; Murray et al., 2021), with modeled trends disagreeing with those derived from  
53 observationally constrained methods (Stevenson et al., 2020). Variables such as the photolysis  
54 frequency of O<sub>3</sub> (JO<sup>1</sup>D) (Nicely et al., 2020), the NO<sub>x</sub> lifetime (NO<sub>x</sub> = NO + NO<sub>2</sub>), and the oxidation  
55 efficiency of VOCs (Murray et al., 2021) contribute to these inter-model variations in OH. Using  
56 Gaussian emulation, Wild et al. (2020) found that the relative importance of drivers of OH variability  
57 differed widely among three CTMs. Likewise, the response of OH to the El Niño Southern Oscillation  
58 (ENSO), the dominant mode of OH variability on monthly and seasonal timescales (e.g. Anderson et al.,  
59 2021; Turner et al., 2018), and other modes of internal climate variability can vary widely among models  
60 (Anderson et al., 2021).

61  
62 Despite this need for better constraints, observations of tropospheric OH are limited. The hydroxyl  
63 radical has a lifetime of approximately 1s (Mao et al., 2009), resulting in large spatial heterogeneity in  
64 both the horizontal and vertical. This spatial heterogeneity is further caused by the large variation in the  
65 relative importance of drivers of OH loss and production in different regions of the atmosphere (e.g.  
66 Spivakovsky et al., 2000; Lelieveld et al., 2016). A strategic, representative in situ observational network  
67 is therefore unfeasible. As a result, observations of OH are generally limited to intensive field campaigns  
68 (Miller and Brune, 2022) that have narrow spatial and temporal coverage. While remotely-sensed OH  
69 observations are available, those from satellites are limited to the stratosphere (e.g., Pickett et al.,  
70 2008), while ground-based observations of total column OH are dominated by the stratospheric  
71 contribution (e.g., Burnett and Minschwaner, 1998).

72  
73 Reference gases with well-characterized sources and an OH sink, such as methyl chloroform (MCF), can  
74 be used to infer OH abundance (Lovelock, 1977). This methodology, however, generally yields no  
75 information on spatial heterogeneity beyond the hemispheric scale (e.g., Montzka et al., 2011; Rigby et  
76 al., 2017; Naus et al., 2019), although there has been recent success when using three dimensional  
77 inversion techniques (Naus et al., 2021). For MCF in particular, recent declines in tropospheric  
78 abundance will soon dictate the need for a new reference species (Liang et al., 2017).

79  
80 Multiple studies have attempted to constrain OH through the creation of proxies and the application of  
81 satellite retrievals of OH drivers. Murray et al. (2014) showed that global OH strongly correlated with a  
82 combination of JO<sup>1</sup>D, water vapor (H<sub>2</sub>O<sub>(v)</sub>), and the tropospheric sources of reactive nitrogen and carbon  
83 in the GEOS-Chem model. Murray et al. (2021) demonstrated that OH correlated with this proxy in  
84 multiple CTMs, although the relationship differs strongly among models. Miyazaki et al. (2020) created  
85 a data assimilation framework that ingested satellite observations of CO, NO<sub>2</sub>, O<sub>3</sub>, and HNO<sub>3</sub> (nitric acid)  
86 into multiple CTMs. The data assimilation reduced the spread in average OH among the models and  
87 brought the interhemispheric ratio closer to unity, in line with values suggested by MCF observations  
88 (e.g. Patra et al., 2014). These results demonstrate that the incorporation of satellite observations into a  
89 modeling framework can improve the representation of OH. Wolfe et al. (2019) developed a proxy for  
90 OH based on formaldehyde (HCHO) production and loss rates. They applied that proxy to satellite HCHO  
91 observations to estimate OH columns in the remote troposphere, a region where HCHO abundance is  
92 low and the satellite retrievals are reflective of the *a priori* (Zhu et al., 2016). Using machine learning,  
93 chemical transport model output, and retrievals of NO<sub>2</sub> and HCHO, Zhu et al. (2022b) developed a  
94 method to estimate surface OH in North American urban areas. Finally, Pimlott et al. (2022) used a  
95 steady state approximation of OH, including primary production from H<sub>2</sub>O and O<sub>3</sub> and loss from CO, CH<sub>4</sub>,

96 and O<sub>3</sub>, to estimate OH between 600 and 700 hPa using observations from IASI (Infrared Atmospheric  
97 Sounding Interferometer). A logical next step, building on the results of these studies, is the  
98 development of a methodology to constrain OH that ingests multiple satellite retrievals, encompasses  
99 the breadth of OH chemical and dynamical drivers, and spans a significant enough portion of the globe  
100 to inform variability and trends in CH<sub>4</sub> and CO loss.

101  
102 Combining machine learning, chemical transport model (CTM) output, and satellite data has the  
103 potential to constrain tropospheric column OH (TCOH). A variety of machine learning techniques, such  
104 as neural networks (Nicely et al., 2017; Nicely et al., 2020; Kelp et al., 2020), self-organizing maps  
105 (Stauffer et al., 2016), random forest regression (Keller and Evans, 2019), and gradient boosted  
106 regression trees (GBRTs) (Ivatt and Evans, 2020; Zhu et al., 2022b; Anderson et al., 2022) show promise in  
107 helping to solve problems in atmospheric chemistry. In particular, Zhu et al. (2022b) and Anderson et al.  
108 (2022) demonstrated the ability of GBRTs to predict OH from a chemical transport model with  
109 reasonable accuracy. GBRT models (Elith et al., 2008; Chen and Guestrin, 2016) use an ensemble of  
110 decision trees to predict the value of a target based on multiple inputs, even for targets with highly non-  
111 linear dependencies on the inputs.

112  
113 Here, we present a methodology to infer clear sky TCOH in the tropics from space-based observations of  
114 its chemical and dynamical drivers with the goal of assessing the feasibility of our methodology,  
115 identifying potential limitations, and suggesting areas of improvement in the current observational  
116 network. We train a GBRT model using output from a simulation of the NASA GEOS (Goddard Earth  
117 Observing System) model, and then estimate TCOH in the actual atmosphere at the satellite overpass  
118 time using inputs from a suite of satellite retrievals. In Section 2, we describe the methodology for  
119 generating the machine learning model as well as the satellite retrievals used to constrain TCOH. We  
120 then evaluate the suitability of MERRA2 GMI as a training dataset (Sect. 3) and, in Section 4, present a  
121 satellite-constrained OH product for one month from each season. Finally, in Section 5, we explore  
122 potential methodological limitations and benefits, including lack of validation data, the impacts of  
123 observational uncertainties, and the ability to use different satellites and retrievals as inputs to the GBRT  
124 model.

## 125 126 **2 Description of the methodology to generate the GBRT model and of the associated datasets**

127 Our overall aim is to demonstrate the feasibility of our approach to constrain TCOH with satellite-based  
128 observations over broad regional scales. As a first step, we restrict our analysis to latitudes equatorward  
129 of 25° and regions over water. We chose to focus initially on this domain as it has appreciable OH  
130 concentrations and simplified chemistry, as compared to regions with large biogenic and anthropogenic  
131 VOC emissions. Nevertheless, this portion of the atmosphere accounts for 50 – 60% of global CO and  
132 CH<sub>4</sub> loss. In this section, we describe the creation of the machine learning model used to predict TCOH  
133 (Sect. 2.1) for this region as well as the satellite products used as inputs to the machine learning model  
134 (Sect. 2.2).

### 135 136 **2.1 Creation of the TCOH model**

#### 137 **2.1.1 Creation of the GBRT training dataset**

138 For the machine learning model training dataset, we use a subset of output from the MERRA2 GMI  
139 simulation (<https://acd-ext.gsfc.nasa.gov/Projects/GEOSCCM/MERRA2GMI/>). MERRA2 GMI is a 40 year  
140 (1980 – 2019) simulation of the NASA GEOS model run in replay mode (Orbe et al., 2017) with MERRA2  
141 (Modern Era Retrospective analysis for Research and Applications, version 2) meteorology (Gelaro et al.,  
142 2017). The simulation has a resolution of c180 on the cubed sphere (approximately 0.625° longitude by  
143 0.5° latitude) with 72 vertical layers and uses the Global Modeling Initiative (GMI) chemical mechanism

144 (Duncan et al., 2007; Strahan et al., 2007). Output is available at daily- and monthly-averaged resolution,  
 145 as well as instantaneous values at 10:00 and 14:00 LST. These times are within approximately 30  
 146 minutes of the overpass times of the satellites described in Section 2.2. Anderson et al. (2021) and  
 147 Strode et al. (2019) provide detailed information about the simulation, including emissions.

148  
 149 The training target for the machine learning model is TCOH. In Anderson et al. (2022), we developed a  
 150 GBRT parameterization trained on MERRA2 GMI output to predict in situ OH concentrations using 27  
 151 inputs, only a small fraction of which are observable from space. That parameterization, designed to be  
 152 integrated into the GEOS modeling framework, performed better when there was a separate model for  
 153 each month as opposed to one model for all months. While that GBRT model is not appropriate for the  
 154 application described here, we employ a similar approach, creating a separate set of TCOH training  
 155 targets for each month. We use instantaneous OH output from MERRA2 GMI at 14:00 local time for  
 156 each day of a given month across the years 2005 to 2019, a timeframe that maximizes overlap between  
 157 the operational lifetime of the satellites listed in Table 1 and the period of the MERRA2 GMI simulation.  
 158 We omitted data from 2017 to evaluate model performance. For a given month and year, we calculate  
 159 daily tropospheric column values across the grid, filtering out columns where the maximum cloud  
 160 fraction in that column was greater than 30% in order to align the training targets more closely with  
 161 satellite data, where retrievals of some species are often filtered for cloud cover. This yields  
 162 approximately 43,000 valid grid boxes per day. For each year, we then average these values to monthly  
 163 resolution. This results in approximately 600,000 total training targets for each month over the 15-year  
 164 period.

165  
 166 **Table 1:** Input variables to the machine learning model and the corresponding satellite retrieval used to create the  
 167 satellite OH product. Overpass times are ~13:30 LST for all satellites except MOPITT, which has a 10:30 LST  
 168 overpass.

Variable	Satellite retrieval	Original horizontal and temporal resolution	Reference
Total O <sub>3</sub> column	OMI TOMS-Like L3 version 3	0.25° × 0.25°, daily	McPeters et al. (2015)
Tropospheric NO <sub>2</sub> column	OMI GSFC L3 version 4	0.25° × 0.25°, daily	Lamsal et al. (2021)
CO column	MOPITT L3 version 8	1.0° × 1.0°, monthly	Deeter et al. (2019)
HCHO column	OMI SAO L3 version 3	0.1° × 0.1°, daily	González Abad et al. (2015)
H <sub>2</sub> O <sub>(v)</sub> column	AIRS L3 version 6	1.0° × 1.0°, monthly	Susskind et al. (2014)
Sea surface temperature	MUR L4 version 4.2	0.25° × 0.25°, daily	Chin et al. (2017)
Aerosol optical depth at 550 nm	MODIS Aqua L3 collection 6	0.5° × 0.5°, daily	Levy et al. (2013)
H <sub>2</sub> O <sub>(v)</sub> layers: 925 – 850 hPa, 850 – 700 hPa, 700 – 600 hPa, 600 – 500 hPa, 500 – 400 hPa, 400 – 300 hPa, and 300 - 250 hPa	AIRS L3 version 6	1.0° × 1.0°, monthly	Susskind et al. (2014)
Solar zenith angle	N/A		
Latitude	N/A		

169  
 170 We selected the input variables for the machine learning model (Table 1) based on their relevance to OH  
 171 chemistry and variability as well as our current ability to observe the variable with satellites.  
 172 Performance was similar for a model including total column ozone only and for a model also including  
 173 the tropospheric column. We therefore use total column ozone because of the uncertainties inherent in

174 separating the column into two parts in the satellite retrieval. We chose the water vapor layers to  
175 correspond with the Atmospheric Infrared Sounder (AIRS) layers product. Layers are averages over the  
176 indicated pressure range, and we denote the layer names by the highest pressure in that range. We  
177 include sea surface temperatures (SST) as a proxy for the Indian Ocean Dipole and ENSO, which has a  
178 strong impact on OH variability in the tropics (Anderson et al., 2021; Turner et al., 2018; Naus et al.,  
179 2021). In addition, we include latitude and solar zenith angle as previous work has shown that these  
180 variables can explain a large fraction of the spatial OH variability (Duncan et al., 2000; Anderson et al.,  
181 2022).

182  
183 We sampled the MERRA2 GMI output to create the training dataset in the same manner as for the TCOH  
184 targets. The inputs to the machine learning model each correspond to the same model column as the  
185 OH target. All column values are instantaneous and taken from 14:00 to correspond with satellite  
186 overpass times, except for CO, which is for 10:00, near the Measurement of Pollution in the  
187 Troposphere (MOPITT) overpass time. Model performance was similar when using CO output at 14:00  
188 and 10:00, likely because of limited diurnal variability in CO column in the study region. SSTs are  
189 monthly averages of 24-hour averaged values, and we calculated solar zenith angle at the surface for  
190 noon on the 15<sup>th</sup> of a given month.

### 191 192 **2.1.2 Creation and tuning of the GBRT model**

193 We used the XGBoost package (Chen and Guestrin, 2016) version 0.81 in Python version 3.6 to create a  
194 GBRT model of TCOH for each month using the training datasets from MERRA2 GMI. For each month,  
195 we used 90% of the dataset for model training and the remainder for model validation. As mentioned in  
196 Section 2.1.1, we also used MERRA2 GMI output from 2017, which was omitted from the training  
197 dataset, as further validation.

198  
199 To maximize parameterization performance while also balancing the potential of overfitting, we tuned  
200 hyperparameters, including the learning rate, the maximum tree depth, and the number of trees. We  
201 chose hyperparameter values that minimized the parameterization root mean square error (RMSE) of  
202 the training dataset. We set the learning rate, which controls the magnitude of change when adding a  
203 new tree, to 0.1, while we varied the maximum tree depth and number of trees from 6 to 22 and from  
204 10 to 150, respectively. For both maximum tree depth and number of trees, RMSE initially dropped  
205 significantly with increasing value, representing sharp improvement in parameterization performance.  
206 RMSE values eventually plateaued, increasing parameterization runtime without noticeably improving  
207 performance. A combination of a maximum tree depth of 18 and 100 trees balanced performance with  
208 model training and run time.

209  
210 To determine whether the inputs to the machine learning model improved or hindered performance, we  
211 performed a “leave one out” analysis. Using 5-fold cross validation, we retrained the model, individually  
212 omitting each of the inputs, to determine the percent difference between the mean RMSE of the 5 folds  
213 for the model without a specific input and one including all inputs. Omitting the inputs listed in Table 1  
214 lead to increases in the RMSE, suggesting that each is necessary for improved model performance. As a  
215 result of this analysis, we do not use water vapor layers for pressures less than 300 hPa because these  
216 decreased model performance.

217  
218 Finally, we found that it was not necessary to apply satellite averaging kernels and shape factors to the  
219 training dataset. Of the satellite retrievals used in this work (discussed in Sect. 2.2 and listed in Table 1),  
220 only CO, HCHO, and NO<sub>2</sub> could require convolving the model with the averaging kernel. Shape factors  
221 for the OMI NO<sub>2</sub> retrieval are determined from a similar setup of the GEOS model, also employing the

222 GMI chemical mechanism and MERRA2 meteorology. Applying the satellite shape factors to the  
223 simulation discussed here would therefore not result in significant changes in the modeled NO<sub>2</sub>  
224 (Anderson et al., 2021). To test whether it is necessary to apply the averaging kernels for CO and HCHO,  
225 we created a separate training dataset, where we convolved the daily MERRA2 GMI output with the  
226 averaging kernel and a priori from the level 2 data for both species for February 2005 - 2019. All other  
227 inputs were kept the same. We then retrained the model with these adjusted CO and HCHO variables.  
228 When we applied the satellite data to the model for February 2017, as described in Section 4, the  
229 resulting TCOH differed by less than 1% on average from the model that did not include averaging kernel  
230 information. This level of uncertainty is significantly smaller than the other uncertainties discussed in  
231 Section 5, so we do not include averaging kernels in our analysis.

232

## 233 **2.2 Description of satellite products**

234 To create the observationally-constrained OH product, we use multiple satellite retrievals, listed in Table  
235 1 and briefly described here. Each instrument is located onboard a polar orbiting satellite that provides  
236 near global coverage daily. For each satellite retrieval, we use the level 3 gridded product, with the  
237 exception of SST which is level 4. Where necessary, we regridded the retrieval to a common horizontal  
238 grid with a resolution of 1.0° × 1.0° and averaged to the monthly scale.

239

240 We use these resolutions because, in the study domain, individual pixel retrievals, particularly of NO<sub>2</sub>  
241 and HCHO, are frequently at or below detection limits (González Abad et al., 2015; Lamsal et al., 2021),  
242 necessitating averaging to relatively coarse temporal and spatial scales. [The study domain partially  
243 mitigates limitations of the 1.0° × 1.0° resolution, as spatial heterogeneity of the relevant species is  
244 generally much lower over the remote tropical oceans than over land.](#) Missing data due to cloud cover  
245 and the Ozone Monitoring Instrument (OMI) row anomaly further increase the need for monthly-scale  
246 averaging. While other satellites, such as OMPS (Ozone Mapping and Profiler Suite) and TROPOMI  
247 (Tropospheric Monitoring Instrument), provide retrievals with increased signal to noise ratios and more  
248 complete data coverage, the satellites used here cover a far longer time period. [Nevertheless, the 1.0°  
249 × 1.0° and monthly resolutions, in combination with the long data record, provide new constraints on  
250 regional trends in TCOH and some aspects of TCOH temporal and spatial variability.](#)

251

252 We use retrievals of three species – HCHO, O<sub>3</sub>, and NO<sub>2</sub> – from OMI, an ultraviolet-visible spectrometer  
253 located onboard the Aura satellite, which has an overpass of approximately 13:30 local solar time (LST).  
254 We use the Smithsonian Astrophysical Observatory (SAO) version 3 HCHO retrieval (González Abad et  
255 al., 2015). Wolfe et al. (2019) found that this retrieval captured the variability of the HCHO columns in  
256 the remote atmosphere observed during the Atmospheric Tomography (ATom) campaign with little bias.  
257 For total column O<sub>3</sub>, we use the TOMS-like (Total Ozone Mapping Spectrometer) retrieval version 3  
258 (McPeters et al., 2015), which agrees with ground-based and other satellite observations within  
259 approximately 1% (Labow et al., 2013). Finally, we use the Goddard Space Flight Center version 4 NO<sub>2</sub>  
260 tropospheric column retrieval (Lamsal et al., 2021). While previous studies have thoroughly evaluated  
261 this retrieval in more polluted atmospheres (e.g., Lamsal et al., 2014; Choi et al., 2020), evaluation in the  
262 remote tropical atmosphere, as defined in this study, is limited.

263

264 For water vapor and aerosol optical depth (AOD) at 550 nm, we use retrievals from AIRS and the  
265 Moderate Resolution Imaging Spectroradiometer (MODIS) instruments, respectively, both located  
266 onboard the Aqua satellite with an overpass of approximately 13:30 LST. We use the total column water  
267 vapor standard physical retrieval as well as the 7 water vapor layers listed in Table 1 (Suskind et al.,  
268 2014). Multiple studies have evaluated the accuracy of the AIRS H<sub>2</sub>O<sub>(v)</sub> column and layers retrievals in  
269 the remote tropical atmosphere, finding bias of 5% or less and high correlation against both remote and

270 *in situ* observations (Bedka et al., 2010;Anderson et al., 2016;Pérez-Ramírez et al., 2019). We use  
271 collection 6 of the dark target MODIS AOD retrieval at 550 nm, which is highly correlated with  
272 observations from the AERONET network over the ocean (Levy et al., 2013).

273  
274 We also use retrievals of CO from MOPITT, which is onboard the Terra satellite with an overpass of  
275 10:30 LST. We use the version 8 retrieval that includes both near and thermal infrared radiances (Deeter  
276 et al., 2019). CO retrievals from MOPITT in the remote tropics generally agree with ground-based  
277 remotely-sensed observations within 10% (Hedelius et al., 2019;Buchholz et al., 2017).

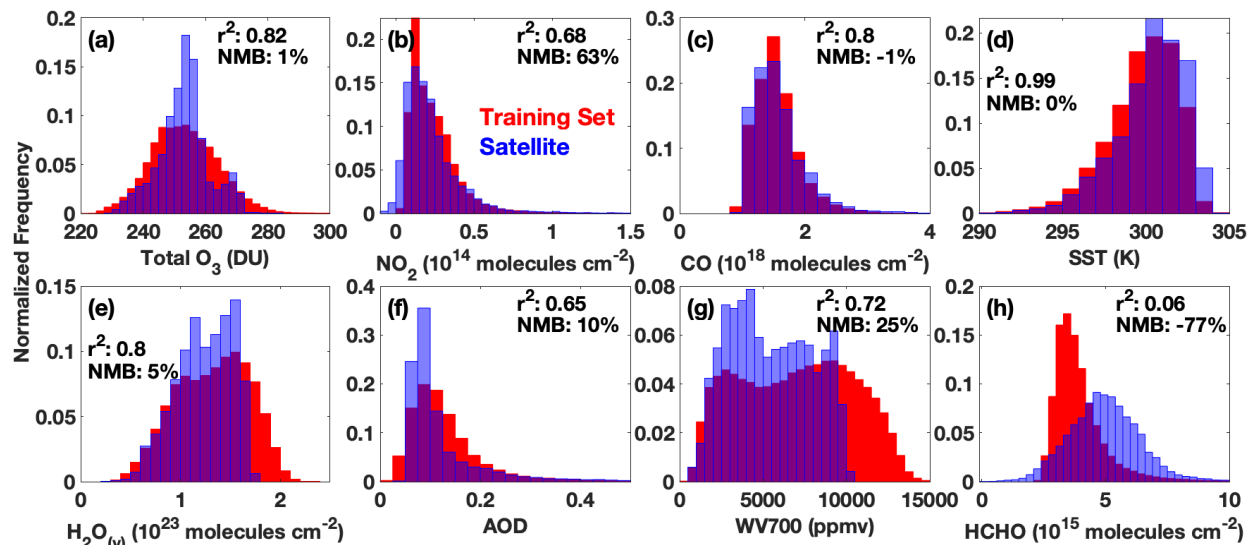
278  
279 Finally, we use SSTs from the Multi-scale Ultra-high Resolution (MUR) analysis, which combines  
280 nighttime SST observations from multiple satellite platforms, including MODIS, as well as *in situ*  
281 observations and agrees with other SST analyses within 0.36° C (Chin et al., 2017).

### 282 **3 Evaluating the Suitability of the MERRA2 GMI Simulation as a Training Dataset**

284 Before generating the GBRT model to predict TCOH, we first demonstrate that the MERRA2 GMI  
285 simulation is suitable to use as a training dataset. Because of the paucity of *in situ* observations of OH  
286 over most of the globe, we necessarily use output from an atmospheric chemistry model to train the  
287 machine learning model. The atmospheric chemistry model output must reasonably capture the  
288 distribution, magnitude, and ENSO-related variability of OH and the drivers listed in Table 1, as GBRT  
289 models are unable to extrapolate beyond the photochemical environments on which they are trained  
290 (Anderson et al., 2022).

#### 291 **3.1 Comparison of the Distribution and Magnitude of Simulated OH Drivers to Observations**

292 Simulated OH from MERRA2 GMI agrees with observations over the remote ocean within the  
293 instrumental uncertainty. Anderson et al. (2021) compared MERRA2 GMI output to *in situ* observations  
294 from the first two deployments of ATom, finding modest correlation ( $r^2$  values between 0.3 and 0.78  
295 depending on the hemisphere and season) between observations and the model. The average  
296 normalized mean bias was on the order of 20%, a slight high bias but within the  $2\sigma$  observational  
297 uncertainty of 35%. Agreement was highest in the remote atmosphere, whereas the largest error was in  
298 regions of fresh, continental outflow off the coasts of South America and New Zealand.  
299  
300



301 **Figure 1:** Comparison of the normalized distributions of the training dataset (red) for the February model and  
 302 satellite observations of the indicated species for February 2017 (blue). Purple indicates regions of overlap. We  
 303 use H<sub>2</sub>O<sub>(v)</sub> at 700 hPa as an example for all H<sub>2</sub>O<sub>(v)</sub> layers. Distributions of the other H<sub>2</sub>O<sub>(v)</sub> layers are shown in Figure  
 304 S1. We also indicate the  $r^2$  of the correlation between MERRA2 GMI output for February 2017 and the  
 305 corresponding satellite retrieval as well as the normalized mean bias of that output.  
 306

307 The simulation captures both the observed variability and the magnitude of the majority of GBRT model  
 308 inputs with reasonable fidelity, suggesting that the satellite retrievals highlighted in Section 2.2 are  
 309 suitable inputs for a machine learning model trained on MERRA2 GMI output (Fig.1). Figure 1 compares  
 310 the distribution of the February training dataset created from the MERRA2 GMI simulation for 2005 –  
 311 2019 to the satellite observations of the indicated species for February 2017, a month omitted from the  
 312 training dataset. Distributions of the remaining water vapor layers are shown in Figure S1. In addition,  
 313 correlations between observations and MERRA2 GMI output for February 2017 are shown, as an  
 314 example, in Figures S2 and S3. With the exception of HCHO, distributions of the species are similar  
 315 between the observations and MERRA2 GMI, with the training dataset encompassing the full range of  
 316 almost all species. A GBRT model trained on MERRA2 GMI will therefore likely not have to extrapolate  
 317 to photochemical environments on which it was not trained when applied to the satellite data. Further,  
 318 MERRA2 GMI total column O<sub>3</sub>, H<sub>2</sub>O<sub>(v)</sub> column, AOD, CO, and SSTs are all highly correlated ( $r^2$  of 0.65 or  
 319 higher) with their respective satellite observations, and biases are within 10%, on average. Anderson et  
 320 al. (2021) did show that MERRA2 GMI CO columns demonstrate biases of opposite sign in the Northern  
 321 and Southern Hemispheres, however.  
 322

323 Agreement between MERRA2 GMI and satellite observations for NO<sub>2</sub>, HCHO, and the H<sub>2</sub>O<sub>(v)</sub> layers is  
 324 more variable than for the other species. While modeled NO<sub>2</sub> is moderately correlated with  
 325 observations ( $r^2 = 0.68$ ) with relatively similar distributions, MERRA2 GMI has a NMB of 63%. This  
 326 disagreement is most pronounced at low column values, however, where observational uncertainty is  
 327 large. Further, Anderson et al. (2021) demonstrated distinct regions of bias in NO<sub>2</sub> related to biomass  
 328 burning and lightning emissions. Modeled HCHO, on the other hand, is not correlated with observations  
 329 and is biased low by -77%. Modeled water vapor layers are all modestly correlated with observations ( $r^2$   
 330 of 0.64 or greater) but vary in their bias, with the 925, 850, 700, and 300 hPa layers biased within 30%  
 331 and the remaining layers biased up to 71%.  
 332



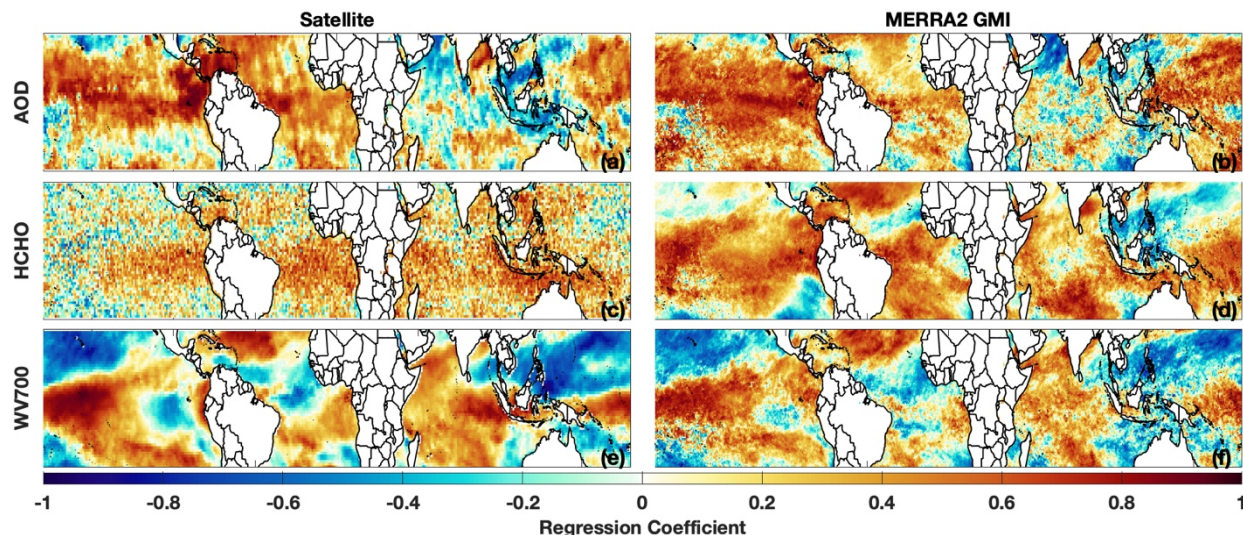
333 The satellite product is insensitive to the differences between the HCHO distribution of the satellite and  
334 training dataset highlighted in Figure 1. To determine the effects of the difference in HCHO distribution,  
335 we extended the training dataset to cover the full time period of the MERRA2 GMI simulation (1980 –  
336 2019) and then subsampled the resultant data to match the satellite HCHO distribution. Extending the  
337 training dataset to 1980 allows for the subsampled training dataset to have a similar size (~600,000  
338 points) as the original training set. We then created a new machine learning model using this sub-  
339 sampled dataset and calculated OH fields for Feb. 2017 using the satellite inputs from Table 1. We  
340 compared this to the TCOH field calculated from a model using the original training dataset, finding  
341 agreement within 5%. Similarly, the satellite-constrained TCOH product discussed in Section 4.2 differs  
342 by only 3% on average from one determined with a GBRT model that excludes HCHO as an input,  
343 suggesting the limited impact of potential errors in the MERRA2 GMI HCHO distribution on model  
344 performance. These uncertainties are small in comparison to that resulting from uncertainties in the  
345 NO<sub>2</sub> and HCHO satellite retrievals discussed in Section 5.2. If the uncertainty of the satellite inputs  
346 decreases, as retrievals and instruments improve, then it will become necessary to more closely align  
347 the training and observed HCHO distributions.

348  
349 Finally, because NO<sub>2</sub> and HCHO have the largest differences between satellite observations and the  
350 training dataset, we trained a separate machine learning model to predict TCOH, omitting these two  
351 species as inputs. When this model was evaluated using the independent MERRA2 GMI output  
352 described in Section 4.1, the NRMSE was 10.1%, a more than factor of 2 degradation in performance as  
353 compared to the baseline model. This suggests that omitting these species from the machine learning  
354 model would result in a greater uncertainty in the final TCOH product than that which results from the  
355 retrieval uncertainties and the potential discrepancies between observations and the training dataset.

356  
357 **3.2 Evaluation of the simulated ENSO-related variability of OH drivers**  
358 Because ENSO is the dominant mode of OH variability (Anderson et al., 2021; Turner et al., 2018), the  
359 training dataset must also capture the ENSO-related variability of the GBRT model inputs. Anderson et  
360 al. (2021) demonstrated that the correlation of columns of CO, H<sub>2</sub>O<sub>(v)</sub>, and to a lesser extent NO<sub>2</sub>, from  
361 the MERRA2 GMI simulation with the Multivariate ENSO Index (MEI) (Wolter and Timlin, 2011) agreed  
362 closely with correlations of the corresponding species for observations from MOPITT, AIRS, and OMI.  
363 Unsurprisingly, based on the strong correlation and low bias of MERRA2 GMI SSTs with observations, the  
364 simulation also captures the relationship between SSTs and ENSO. The simulation therefore sufficiently  
365 captures the ENSO-related variability of these species to act as training data for the GBRT model. We  
366 now evaluate this relationship for the remaining GBRT model inputs.

367  
368 The MERRA2 GMI-simulated ENSO-related variability of AOD and the various water vapor layers also  
369 agrees well with observations. Figures 2 and S4 show the correlation of AOD, HCHO, and the various  
370 H<sub>2</sub>O<sub>(v)</sub> layers with the MEI for the satellite retrievals and MERRA2 GMI. MERRA2 GMI captures the  
371 general distribution and magnitude of correlation between AOD and ENSO, despite the low optical  
372 depths over much of the domain. There are some regional differences, however, particularly in the  
373 eastern Southern Hemispheric Pacific. For the H<sub>2</sub>O<sub>(v)</sub> layers, the simulation underestimates the  
374 magnitude of the correlation in some areas, but in general, there is excellent agreement for all layers  
375 throughout the troposphere. This suggests that, despite the high bias discussed above, including the  
376 H<sub>2</sub>O<sub>(v)</sub> layers could provide important, vertically-resolved information to the machine learning model.

377



378  
 379 **Figure 2:** Distribution of the regression coefficient of a linear least squares fit of the indicated variable against the  
 380 MEI for the respective satellite retrieval (a, c, and e) and MERRA2 GMI (b,d, and f) for February. Regressions of  
 381 AOD are for 2010 to 2019, the years for which we have a one-degree, gridded satellite product, while HCHO and  
 382 water vapor 700 hPa are for 2005 to 2019. Satellite data are on a  $1^\circ \times 1^\circ$  grid while model output is at the native  
 383 model resolution.

384 Modeled accuracy of the HCHO-ENSO relationship is more difficult to assess. While both the OMI  
 385 retrieval and MERRA2 GMI demonstrate broad regions of anti-correlation between HCHO and ENSO, the  
 386 correlations with OMI HCHO are weaker and noisier than for the other satellite retrievals. Over much of  
 387 the domain, HCHO abundance is low, often at or below the retrieval detection limit, suggesting that the  
 388 HCHO retrieval might not be of sufficient quality to capture ENSO-related variability. We investigate the  
 389 impacts of the HCHO observational uncertainty in Section 5.

390  
 391 Finally, because we use total column  $O_3$  as an input to the GBRT model, we do not evaluate the  
 392 relationship between ENSO and  $O_3$ , as the stratosphere dominates the  $O_3$  column and the ENSO-related  
 393 variability is mostly confined to the troposphere. Oman et al. (2013) found that a GEOS CCM simulation  
 394 and a combination of  $O_3$  retrievals from the Microwave Limb Sounder (MLS) and the Tropospheric  
 395 Emission Spectrometer (TES) exhibited similar ENSO-related variability in the middle and upper  
 396 troposphere, demonstrating that simulations in the GEOS framework can capture this relationship. If a  
 397 TES-like satellite retrieval were currently available, it could be a valuable contributor to the GBRT model  
 398 described here, as it would provide vertically-resolved information about one of the primary drivers of  
 399 OH production.

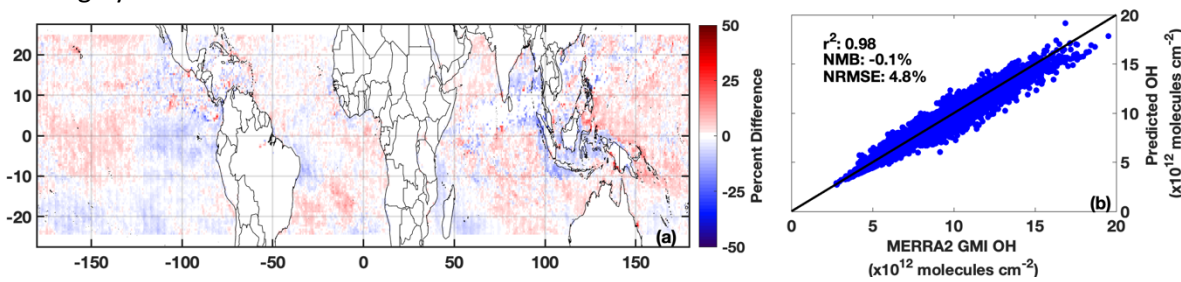
#### 400 401 **4 Tropical tropospheric column OH constrained with observations of its drivers**

402 We now demonstrate the ability of the GBRT model to determine TCOH. First, we show that the GBRT  
 403 model can reproduce MERRA2 GMI modeled TCOH from a year independent of the training dataset, a  
 404 so-called “hold out set” (Sect. 4.1). We then input satellite data from one month from each season into  
 405 the GBRT model to evaluate the realism of the calculated TCOH fields (Sect 4.2).

#### 406 407 **4.1 Evaluation with an independent year from MERRA2 GMI**

408 The machine learning model is able to capture both the magnitude and the variability of TCOH across  
 409 each season when applied to MERRA2 GMI output from 2017, a year independent of the training  
 410 dataset. For August 2017 (Fig. 3b), the predicted TCOH is highly correlated with MERRA2 GMI ( $r^2$  of

411 0.98). TCOH from the machine learning model agrees with the CTM simulation within 4.8% on average.  
412 The overall normalized mean bias (NMB) is negligible (-0.1%), although there are some regions of  
413 coherent bias (Fig. 3a). Results are similar for February, May, and October 2017 (Fig. S5). The  
414 normalized root mean square error for each of these months is comparable to that found for a GBRT  
415 parameterization of OH created with a similar methodology that included 27 inputs (Anderson et al.,  
416 2022). This suggests that limiting inputs to model variables observable from space does not degrade the  
417 ability of the machine learning model to predict TCOH. The low bias and high correlation between the  
418 GBRT and MERRA2 GMI TCOH for all four months examined here also suggests that any potential  
419 overfitting by the GBRT model is minimal.



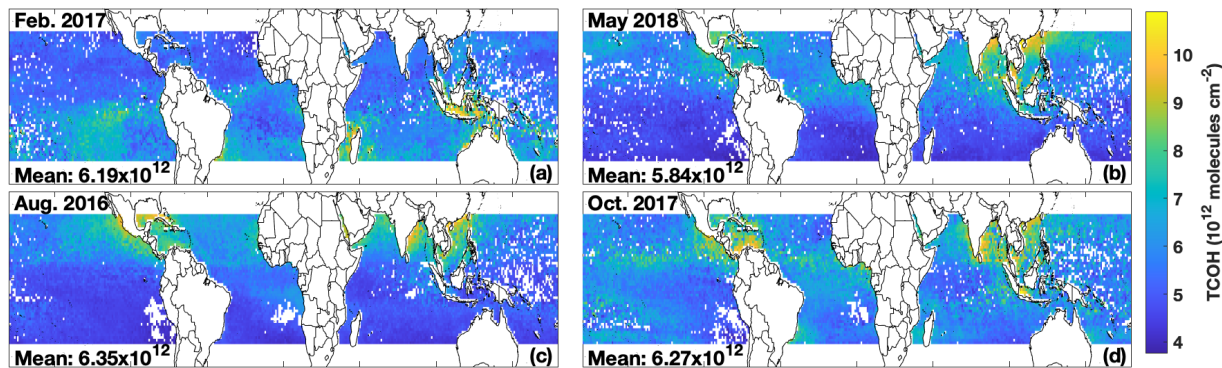
420  
421 **Figure 3:** Percent difference between TCOH predicted by the machine learning model and that from MERRA2 GMI  
422 for August 2017, a month and year omitted from the training dataset (a). A regression of the machine learning TCOH  
423 against MERRA2 GMI for the same month (b). The  $r^2$  of a linear, least squares regression, along with the normalized  
424 mean bias (NMB) and normalized root mean square error (NRMSE), are also indicated.

#### 425 4.2 TCOH from satellite observations of its drivers

426 We now apply satellite data from the four months corresponding to the ATom campaign (Aug. 2016,  
427 Feb. 2017, Oct. 2017, and May 2018) to the GBRT model to determine TCOH fields across the tropics.  
428 More details about ATom as well as evaluation of the GBRT model with ATom observations are in  
429 Section 5. We use the satellite observations listed in Table 1, all of which have been averaged to the  
430 monthly scale and to a  $1^\circ \times 1^\circ$  horizontal resolution. We include only grid boxes with observations for  
431 all GBRT model inputs and where those observations are within the range of the corresponding inputs  
432 from the training dataset. Because the satellite inputs for most species exclude grid boxes with a cloud  
433 fraction greater than approximately 30%, the product presented here represents predominantly clear  
434 sky conditions.

435  
436 The GBRT model and multi-satellite inputs yield TCOH fields that are geophysically credible based on our  
437 current understanding of OH photochemistry. Although the domain-wide average changes little with  
438 season, with a minimum of  $5.84 \times 10^{12}$  molecules/cm<sup>2</sup> in May 2018 and a maximum of  $6.35 \times 10^{12}$   
439 molecules/cm<sup>2</sup> in August 2016, the spatial distribution varies widely among the four months (Fig. 4). In  
440 both Feb. 2017 and Aug. 2016, TCOH minimizes in the winter hemisphere, consistent with lower OH  
441 production due to low insolation. The reverse is true for the summer hemisphere. In addition, TCOH  
442 maximizes in regions with strong continental outflow and along coastlines, regions likely to be impacted  
443 by anthropogenic and biomass burning emissions of OH drivers.

444



445  
446 **Figure 4:** TCOH calculated with the machine learning model using satellite inputs for the months of each ATom  
447 deployment: Feb. 2017 (a), May 2018 (b), Aug. 2016 (c), and Oct. 2017 (d). The mean, domain-wide TCOH value in  
448 molecules/cm<sup>2</sup> for each month is also indicated.

449 In general, TCOH from the multi-satellite product differs in both magnitude and distribution from the  
450 MERRA2 GMI simulation. For example, for Feb. 2017, mean MERRA2 GMI TCOH is  $6.96 \times 10^{12}$   
451 molecules/cm<sup>2</sup>, 12% higher than the satellite product (Fig. S6). This is consistent with the comparison to  
452 *in situ* observations discussed in Section 3.1 where MERRA2 GMI overestimates ATom observations by  
453 ~20% and underestimates CH<sub>4</sub> lifetime, suggesting that the satellite product is again of reasonable  
454 magnitude. While understanding the satellite/model differences in TCOH is beyond the scope of this  
455 work, we consider the variety in TCOH spatial distributions generated by the GBRT model to be  
456 promising. The difference between the satellite-constrained product and MERRA2 GMI lends some  
457 confidence that the GBRT model is not overfit or “tied” to geographic determiners in the training  
458 dataset, but rather, is sensitive to variations in the chemical and dynamical drivers of OH. These results  
459 all suggest that the methodology presented here can produce a reasonable satellite TCOH product in the  
460 tropics, with values and distributions independent of the chemistry model used to create the GBRT  
461 model.

## 462 463 **5 Understanding and mitigating potential challenges in using this methodology to constrain TCOH**

464 In this section, we outline possible limitations of the machine learning methodology and the current  
465 observational network of the GBRT model inputs and provide potential means to mitigate these  
466 limitations where necessary. In section 5.1, we discuss the current lack of sufficient *in situ* observations  
467 to thoroughly evaluate the methodology, highlighting this point by validating the GBRT model with data  
468 from the ATom campaign. In section 5.2, we investigate the impacts of random retrieval errors in  
469 satellite retrievals on the TCOH product, while in section 5.3, we evaluate the impacts on TCOH when  
470 using different satellite retrievals as inputs.

### 471 472 **5.1 Insufficient *in situ* observations for thorough independent evaluation**

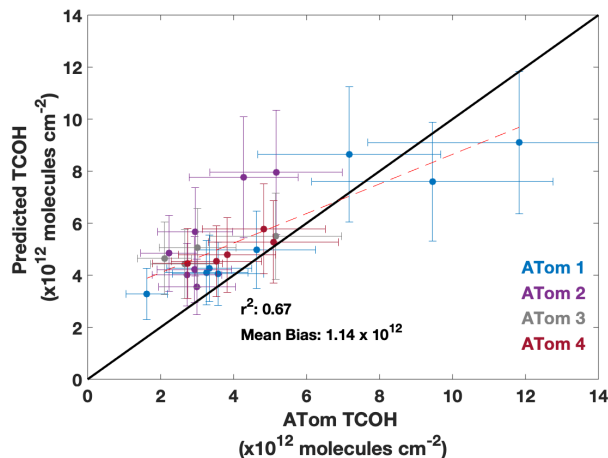
473 While we demonstrated in Section 4.1 that TCOH calculated with the GBRT model agrees closely with a  
474 hold-out set from MERRA2 GMI, it is also important to demonstrate that the GBRT model can replicate  
475 observed TCOH from the actual atmosphere. Because the satellite TCOH product shown in Figure 4 is  
476 monthly and at a  $1^\circ \times 1^\circ$  resolution, however, there are no observations with which to evaluate the  
477 product. We can test the ability of the GBRT model to reproduce observed TCOH from field campaigns,  
478 however, assuming there are concomitant observations of the input species listed in Table 1. The  
479 additional need for tropospheric column values of many of these species severely limits the datasets  
480 available for validation. To our knowledge, the ATom campaign is the only source of the required inputs  
481 with enough observations to attempt a limited validation.

482



483 During ATom (Thompson et al., 2022), scientists measured a suite of air quality and climate relevant  
 484 trace gases and aerosols throughout the atmosphere above the remote Pacific and Atlantic. ATom took  
 485 place in four parts: ATom 1 (July – August 2016), ATom 2 (January – February 2017), ATom 3 (September  
 486 – October 2017), and ATom 4 (April – May 2018). During each deployment, flights consisted of a series  
 487 of ascents and descents across all tropical latitudes over the Pacific and Atlantic Oceans. This allows for  
 488 the calculation of tropospheric column content of the observed species and evaluation of the machine  
 489 learning model across most latitudes of our study domain and across all seasons.

490  
 491 To evaluate the GBRT model performance, we calculated TCOH using a modified GBRT model and  
 492 observations from the ATom deployments as inputs. We then compared the values to the observed OH  
 493 columns. To calculate the column values from the observations, we averaged data into 25 hPa pressure  
 494 bins for each ATom profile. We filled in missing data using a log-linear interpolation and then integrated  
 495 the column. Our analysis here includes only profiles with observations of all necessary species, that  
 496 spanned at least 700 hPa, and where less than 25% of the pressure bin values were interpolated. We  
 497 also omitted any profiles that had pressure bins with negative OH values. In addition, we restrict our  
 498 analysis to latitudes within 25° of the equator and profiles conducted between 12:00 and 15:00 LST.  
 499 Values for total column O<sub>3</sub>, AOD, and SSTs, for which there were no observations during ATom, were  
 500 taken from the MERRA2 GMI simulation from the grid box closest to the center of the respective profile.  
 501 Because ATom profiles did not span the entire tropospheric column, we trained a separate GBRT model  
 502 where OH and all tropospheric column input variables were substituted with columns spanning 990 –  
 503 250 hPa, the median range of ATom profiles. This allows for a more direct comparison between  
 504 observed and modeled TCOH. The spatial distribution of the valid ATom columns and the corresponding  
 505 columns calculated with the GBRT model are shown in Figure S7.  
 506



507  
 508 **Figure 5:** Regression of TCOH observed from the ATom deployments against that predicted from the GBRT model.  
 509 Error bars represent the 2 $\sigma$  observational uncertainty as reported in Brune et al. (2020) and the GBRT uncertainty  
 510 described in Section 5.2. The  $r^2$  of a linear least squares fit and the mean bias are also shown.

511 The GBRT model captures the variability of the observed TCOH, and, while there is a modest overall high  
 512 bias, the median normalized absolute error of 28.3% is within observational uncertainty. When applied  
 513 to all ATom deployments, predicted TCOH is correlated with the observations with an  $r^2$  of 0.67 and a  
 514 mean bias of  $1.14 \times 10^{12}$  molecules/cm<sup>2</sup> (Fig.5). Many of the data points agree within the combined  
 515 modeled and observational uncertainty. The  $r^2$  values for individual deployments are 0.88 for ATom 1,  
 516 0.73 for ATom2, and 0.78 for ATom 3 and 4. The level of agreement between observed and predicted  
 517 OH is comparable or better than that of other methods to infer OH from space. For example, Pimlott et

518 al. (2022) found an  $r$  of 0.78 ( $r^2 = 0.61$ ) when estimating ATom OH using a steady state approach, with  $r$   
519 values ranging from 0.51 to 0.85 ( $r^2$  of 0.26 to 0.72) for the different deployments. The level of  
520 agreement we show here therefore demonstrates the validity of the machine learning method to  
521 capture the variability of OH.

522  
523 The source of the model/measurement disagreement, with over- and underprediction at low and high  
524 column content respectively, is unclear, although there are multiple potential error sources. For  
525 example, a typical profile taken during ATom spanned 300 – 400 km in latitude, disconnecting the top  
526 and bottom of the profile in space. This is in contrast to the data used to train the model, which were  
527 vertical columns over one location. This could lead to a degradation in model performance when  
528 applied to ATom, since the columns are not directly analogous to the training dataset. These effects are  
529 likely limited because ATom observations are in the remote atmosphere, where the spatial distribution  
530 of relevant species is likely to be more homogeneous than over land.

531  
532 Further, there is a known interference with the ATom NO<sub>2</sub> observations, suggesting another possible  
533 contributor to disagreement between measured and modeled OH. Because of thermal degradation of  
534 NO<sub>2</sub> reservoir species, such as organic nitrates and peroxyacetyl nitrate, in the instrument inlet, ATom  
535 NO<sub>2</sub> observations are likely biased high (Silvern et al., 2018; Shah et al., 2023; Nault et al., 2015). To test  
536 the potential impact of NO<sub>2</sub> on the predicted OH columns, we applied the ATom observations to a model  
537 that omits NO<sub>2</sub> as an input. Removing NO<sub>2</sub> increases the  $r^2$  to 0.74, decreases the mean bias to  $0.82 \times$   
538  $10^{12}$  molecules/cm<sup>2</sup>, and decreases the median normalized absolute error slightly to 25.7% (Fig. S8).  
539 These improvements in performance suggest that errors in NO<sub>2</sub> could be contributing to the  
540 measurement/model differences. Omitting NO<sub>2</sub> does, however, likely introduce additional errors as NO<sub>x</sub>  
541 compounds are essential to OH production in some regions of the atmosphere. When we apply the hold  
542 out set from MERRA2 GMI to this model, for example, the NRMSE increases by approximately 50%,  
543 highlighting the importance of keeping NO<sub>2</sub> as an input variable.

544  
545 For more certain evaluation of the GBRT model with observations, greater certainty in the in situ NO<sub>2</sub>  
546 observations is needed. Although the in situ observations are insufficient to evaluate the absolute  
547 accuracy of the product, the results presented here demonstrate that a machine learning model trained  
548 on data from a CTM simulation can capture TCOH variability in the actual atmosphere and suggest that  
549 predicted OH columns agree with observations within instrumental uncertainty.

## 550 551 **5.2 Impacts of uncertainties in the satellite retrievals on TCOH**

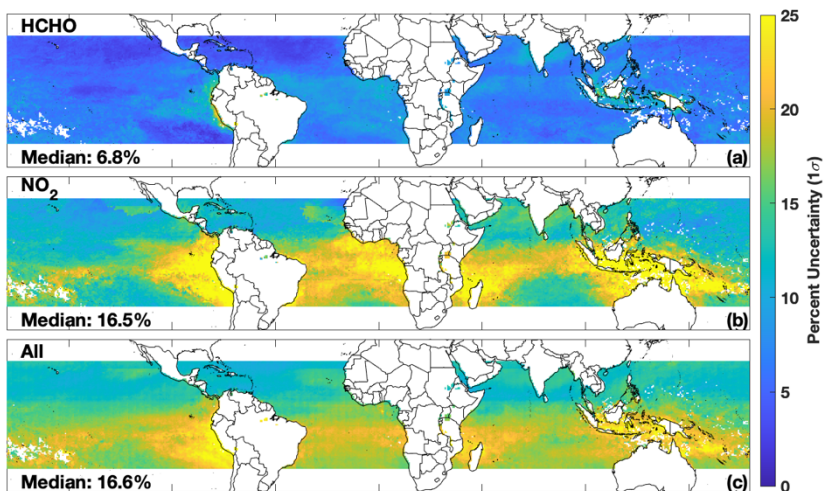
552 In the remote atmosphere where HCHO and NO<sub>2</sub> abundances are low, retrieval uncertainty of an  
553 individual pixel for both species can be on the order of 100% and is often reflective of the *a priori*  
554 (González Abad et al., 2015; Lamsal et al., 2021). Given the importance of these species to the GBRT  
555 model as well as to OH chemistry, it is necessary to determine how the propagation of the retrieval  
556 uncertainties from these and other model inputs impacts the predicted TCOH.

557  
558 We determined the total uncertainty in TCOH from all inputs as well as the resultant uncertainty from  
559 each individual input for Feb. 2017. First, we estimated an average retrieval uncertainty for each input  
560 based on reported values in the retrieval files or from the literature (Table S1). We note that for NO<sub>2</sub>  
561 and HCHO we use a fit uncertainty for a single retrieval. Because we are using monthly-averaged data at  
562  $1^\circ \times 1^\circ$  horizontal resolution, this likely significantly overestimates the actual uncertainty in these  
563 retrievals as the random error from individual pixels will tend to cancel when averaged over such large  
564 spatial and temporal scales. Our results are therefore an upper bound on the estimated TCOH  
565 uncertainty.

566  
567  
568  
569  
570  
571  
572  
573  
574  
575  
576  
577  
578  
579  
580  
581  
582  
583  
584  
585  
586  
587

Next, for each grid box and model input, we created a Gaussian distribution of 2000 values with the modeled value for Feb. 2017 as the mean and the estimated uncertainty as the standard deviation. For each input, we then ran the GBRT model 2000 times to create a distribution of predicted TCOH values for each grid box. The normalized uncertainty in TCOH attributable to a given input is the ratio of the standard deviation of the resultant distribution divided by the mean value. We repeated this process individually for all inputs. In addition, to estimate a total uncertainty in TCOH, we varied all inputs simultaneously with the same Gaussian distributions described above.

Uncertainty from the NO<sub>2</sub> retrieval, and to a lesser extent HCHO, dominates the total uncertainty in the TCOH product but is of a magnitude comparable to that of in situ OH observations. Median TCOH 1 $\sigma$  uncertainty resulting from NO<sub>2</sub> is 16.5%, with maxima in the remote atmosphere in regions where NO<sub>2</sub> columns are low. Median uncertainty in TCOH resulting from HCHO is 7%, averaged over the study domain, despite the large uncertainty in the HCHO retrieval itself. In contrast to NO<sub>2</sub>, uncertainties in TCOH resulting from HCHO maximize in regions with higher HCHO columns (Fig. 6). The magnitude of that uncertainty is likely an overestimate as the actual retrieval uncertainty for HCHO in these regions is significantly lower than the value assumed for the error analysis. In comparison, median TCOH uncertainties resulting from other inputs are 2.9% or less (Figs. S9 and S10). Total TCOH uncertainty is 16.6% and is dominated by the NO<sub>2</sub> uncertainty. This uncertainty analysis is in general agreement with the model feature importance (Supplementary Fig. 11), a measure of the relative importance of GBRT model inputs, where HCHO and NO<sub>2</sub> consistently have the largest values of the satellite inputs.



588  
589  
590

**Figure 6:** Normalized 1 $\sigma$  uncertainty in the satellite TCOH product due to uncertainties in the HCHO (a) and NO<sub>2</sub> (b) retrievals. The combined uncertainty from all input species is shown in panel c.

591 These results demonstrate that the satellite retrieval inputs to the machine learning model are of  
592 sufficient quality to produce a meaningful TCOH data product when averaged over large spatial and  
593 temporal scales. The 2 $\sigma$  uncertainty in TCOH resulting from the uncertainties in these retrievals is on  
594 the order of that reported for in situ OH observations (Brune et al., 2020). As discussed earlier, this is  
595 also likely an upper bound on the uncertainty from random retrieval errors, and uncertainties could be  
596 reduced through further averaging, although at the expense of reduced spatial and temporal resolution.  
597 Improving the satellite retrievals of NO<sub>2</sub> and HCHO in the remote atmosphere, using retrievals with less  
598 noise over the remote atmosphere such as HCHO from OMPS (González Abad et al., 2016), or  
599 incorporating data from satellites with higher resolution, such as TROPOMI, could also reduce the

600 uncertainty in their retrievals and thus in TCOH. As discussed in the next section, however, systematic  
601 biases between satellite retrievals can also lead to uncertainties in the TCOH.

602

### 603 **5.3 Sensitivity of TCOH to different satellite retrievals of GBRT inputs**

604 The satellite retrievals listed in Table 1 provide the benefit of a long record, with data from most  
605 retrievals available from at least 2005 to the present. Such a rich dataset would allow for long-term  
606 trend analysis of TCOH. These instruments are near the end of their life cycle, however, so it is  
607 instructive to see how retrievals from newer satellites impact the predicted TCOH from the GBRT model.  
608 In addition, although these newer satellites, such as TROPOMI, have a significantly shorter observational  
609 record than those in Table 1, TROPOMI also has finer spatial resolution and the added advantage of  
610 providing retrievals for CO, NO<sub>2</sub>, O<sub>3</sub>, HCHO, and H<sub>2</sub>O<sub>(v)</sub>. Using retrievals of multiple species from the  
611 same instrument could negate errors resulting from differences in viewing geometry as well as from  
612 overpass time. Here, we investigate the effects of applying retrievals from TROPOMI to the machine  
613 learning model and compare them to the results from the product described in Section 4, highlighting  
614 potential impacts resulting from instrumental differences as well as those resulting from differences in  
615 retrieval algorithms. The results emphasize the need for thorough retrieval validation in the remote  
616 atmosphere, particularly of NO<sub>2</sub>.

617

#### 618 **5.3.1 Description of TROPOMI and a modified GBRT model**

619 TROPOMI, a successor instrument to OMI, is a spectrometer covering portions of the ultraviolet, visible,  
620 and infrared spectrum (Veefkind et al., 2012). It is located onboard the Sentinel 5 Precursor satellite,  
621 which is polar orbiting and has a local overpass time of approximately 13:30. Horizontal resolution for  
622 the month examined here (May 2018) is as high as 7 km × 3.5 km at nadir. [All TROPOMI retrievals used](#)  
623 [here, unless otherwise indicated, are the reprocessed version 1 products.](#) We have gridded the Level 2  
624 product for each species to a 1° × 1° resolution and averaged the data to the monthly scale, applying the  
625 recommended quality flags and filtering for cloud fraction greater than 30%.

626

627 We use two different retrievals of TROPOMI NO<sub>2</sub> for this analysis. First, we use the KNMI (Royal  
628 Netherlands Meteorological Institute) NO<sub>2</sub> retrieval (van Geffen et al., 2020), which is based on the  
629 DOMINO (Dutch OMI NO<sub>2</sub> product) retrieval developed for the OMI instrument. Wang et al. (2020)  
630 found that this retrieval was biased high when compared to ship-based observations from a MAX-DOAS  
631 instrument over the remote oceans, while Verhoelst et al. (2021) found good agreement between the  
632 retrieval and ground-based observations in Reunion. In addition, we use the MINDS (Multi-Decadal  
633 Nitrogen Dioxide and Derived Products from Satellites) retrieval, which uses the same algorithm as for  
634 the OMI product described in Section 2 (Lamsal et al., 2022). This retrieval has not been evaluated in  
635 the remote tropics.

636

637 We also use TROPOMI retrievals of HCHO, H<sub>2</sub>O<sub>(v)</sub> column, total column O<sub>3</sub>, and CO. The HCHO retrieval  
638 (De Smedt et al., 2018) was found to have a 30% low bias with respect to an OMI retrieval using the  
639 same algorithm due to differences in cloud processing (De Smedt et al., 2021). While evaluation in the  
640 remote tropics is limited, the TROPOMI retrieval does overestimate HCHO in polluted regions (De Smedt  
641 et al., 2021) when compared to ground-based observations. The TROPOMI H<sub>2</sub>O<sub>(v)</sub> (Chan et al., 2022)  
642 retrieval has a slight dry bias with comparison to other satellite products, while the total column O<sub>3</sub>  
643 retrieval (Garane et al., 2019) agrees within 0 – 1.5% with ground-based observations. Finally, the CO  
644 retrieval (Borsdorff et al., 2019) agrees with MOPITT over the oceans within 3% on average (Martínez-  
645 Alonso et al., 2020). TROPOMI does not have an equivalent retrieval of the AIRS H<sub>2</sub>O<sub>(v)</sub> layers.

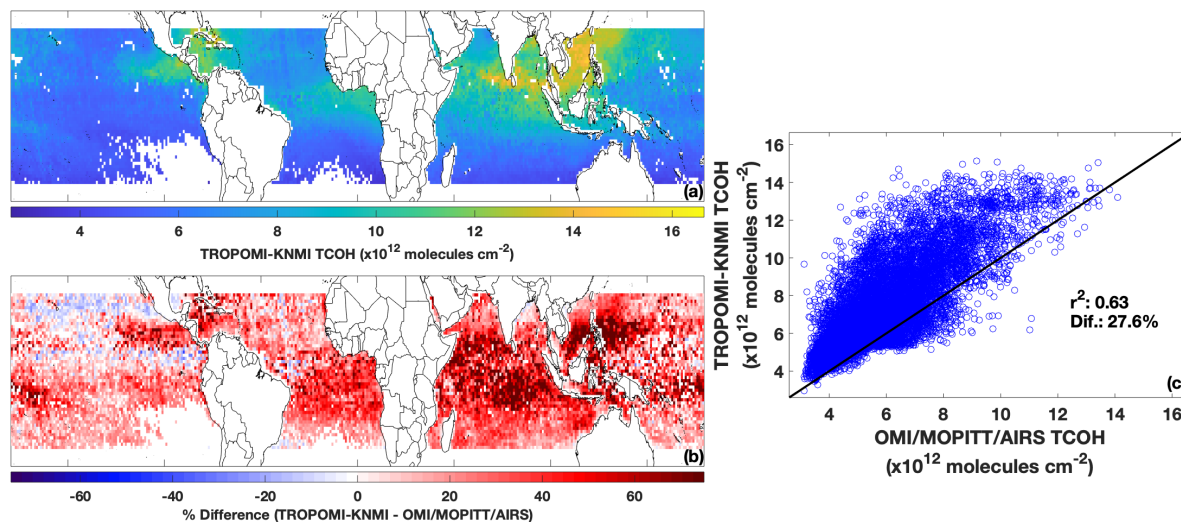
646



647 To calculate TCOH using TROPOMI data, we trained a separate machine learning model using all inputs  
 648 from Table 1 except the water vapor layers, for which there are no TROPOMI retrievals. Removal of the  
 649 layers from the machine learning model does not significantly degrade performance. For example, for  
 650 May 2017, removing the H<sub>2</sub>O<sub>(v)</sub> layers from the model, increases the NRMSE from 5.34% to 5.73% when  
 651 applying the GBRT model to the hold out set. For this new model, we then calculate TCOH using  
 652 TROPOMI data, including the KNMI NO<sub>2</sub> retrieval. For SSTs and AOD, we use the MUR and MODIS  
 653 products respectively. While TROPOMI does have an aerosol product, the UV aerosol index, the  
 654 corresponding output from the MERRA2 GMI simulation is unavailable. We refer to this TCOH as the  
 655 TROPOMI-KNMI product. We have also calculated TCOH using the satellite retrievals in Table 1, except  
 656 for the water vapor layers, using this GBRT model, and refer to that as the OMI/MOPITT/AIRS product.  
 657 We restrict our analysis to May 2018, the only month for which we have TROPOMI water vapor data.  
 658

### 659 5.3.2 TROPOMI data applied to the GBRT model

660 TCOH from the TROPOMI-KNMI product is higher than that from the OMI/MOPITT/AIRS product for May  
 661 2018. Figure 7 shows TCOH calculated from the TROPOMI-KNMI product as well as the percent  
 662 difference between the two products. While there is modest correlation between the two ( $r^2 = 0.63$ ),  
 663 the TROPOMI product is 27.6% higher than the OMI/MOPITT/AIRS product, with higher values across  
 664 almost the entire domain. Differences between the products are most pronounced in the Indian Ocean  
 665 and off the coasts of Indonesia and the Philippines.  
 666



667 **Figure 7:** TCOH for May 2018 determined using TROPOMI inputs, including the KNMI NO<sub>2</sub> retrieval (a). The  
 668 difference between the TROPOMI and multi-satellite product is shown in (b). Panel (c) shows the regression of  
 669 TCOH calculated from TROPOMI against that calculated from retrievals from MOPITT, OMI, and AIRS as well as the  
 670 percent difference between the two TCOH products.  
 671

672 In general, observations from TROPOMI agree with those from the satellites in Table 1, with the  
 673 exception of NO<sub>2</sub> and HCHO. Ozone, H<sub>2</sub>O<sub>(v)</sub>, and CO from TROPOMI are highly correlated ( $r^2$  of 0.85 or  
 674 higher) and agree within 10% on average (Fig. S12) with their respective retrievals from OMI, MOPITT,  
 675 and AIRS. On the other hand, TROPOMI KNMI-NO<sub>2</sub> is systematically higher (145% on average), and  
 676 TROPOMI HCHO is 20% lower than their corresponding OMI retrievals. The higher TCOH from the  
 677 TROPOMI product is consistent with the increase in NO<sub>2</sub>, which would lead to higher secondary  
 678 production of OH. Further, while TROPOMI KNMI-NO<sub>2</sub> is modestly correlated with OMI NO<sub>2</sub> ( $r^2 = 0.61$ ),  
 679 TROPOMI and OMI HCHO are not correlated ( $r^2 = 0.23$ ), highlighting the difficulty of the HCHO retrieval.  
 680 Note that we are not seeking to determine which retrieval, if any, is more accurate. We are highlighting

681 the differences to emphasize the impact that systematic differences in retrieval magnitudes of GBRT  
682 model inputs can have on the resultant TCOH.

683  
684 NO<sub>2</sub> drives the differences between the two TCOH products. To determine the impacts of the different  
685 TROPOMI inputs on the TCOH product, we individually swapped each TROPOMI input into the  
686 OMI/MOPITT/AIRS product, replacing the corresponding input from Table 1. We then determined the  
687 difference in TCOH from the OMI/MOPITT/AIRS product that does not include TROPOMI. While this  
688 method will not yield the exact contribution from a particular retrieval because of the non-linear nature  
689 of OH chemistry, it does yield information about the relative importance of each species. Swapping in  
690 TROPOMI CO, H<sub>2</sub>O<sub>(v)</sub>, and O<sub>3</sub> changed TCOH by less than 2%, while using TROPOMI HCHO increased  
691 TCOH by 3%. In contrast, TROPOMI NO<sub>2</sub> increased TCOH by 29%, showing that the higher TCOH in the  
692 TROPOMI product is driven by differences in NO<sub>2</sub>.

693  
694 The increased TCOH in the TROPOMI product likely results from a combination of differences in the NO<sub>2</sub>  
695 retrieval algorithm as well as instrumental differences. Comparison of the KNMI and MINDS retrievals  
696 illustrate this point. When compared to OMI, the MINDS NO<sub>2</sub> retrieval is 58% higher for May 2018, as  
697 compared to 145% higher for the KNMI retrieval. The closer agreement is unsurprising since the MINDS  
698 NO<sub>2</sub> uses the same retrieval algorithm as for OMI. Substituting the MINDS NO<sub>2</sub> as an input to the  
699 TROPOMI product (TROPOMI-MINDS product) reduces the difference with respect to the  
700 OMI/MOPITT/AIRS product to 18% (Fig. S13). While this is an improvement in agreement, the  
701 differences in TCOH as well as the lack of change in r<sup>2</sup> value still suggest that differences between OMI  
702 and TROPOMI unrelated to the retrieval algorithm account for some of the discrepancy. In addition, the  
703 training dataset does not take TROPOMI averaging kernels and shape factors into account, which could  
704 also contribute to the observed differences.

705  
706 The results here demonstrate the sensitivity of the methodology to any systematic bias in the input  
707 retrievals. As with the random error analysis, the level of uncertainty introduced by these biases is low  
708 enough to allow for a meaningful OH product. Despite these differences, the methodology to determine  
709 TCOH using machine learning that we have presented here still captures the variability in TCOH,  
710 consistent with the ATom evaluation outlined in Section 5.1. To reduce the uncertainty of TCOH, better  
711 evaluation of NO<sub>2</sub> in the remote atmosphere is needed to determine which retrievals, if any, are  
712 accurate.

## 713 714 **6 Discussion and recommendations for future observations**

715 The method of estimating clear-sky TCOH presented here has the potential to increase our  
716 understanding of the atmospheric oxidation capacity. Because of the long record of observations from  
717 MOPITT, OMI, AIRS, and MODIS, we can calculate tropical TCOH from 2005 to the present, and since the  
718 methodology is not constrained to a particular satellite, newer satellite missions could extend the  
719 dataset beyond the end of these instruments' lifetimes. In addition, this methodology will provide sub-  
720 hemispheric information on OH variability, supplementing information available from MCF inversions.

721  
722 The methodology could be expanded to the extra-tropics and over land, allowing for global constraints  
723 on OH. Expansion over land will likely require additional satellite retrievals, like that of isoprene (Wells  
724 et al., 2020), in regions with more complex VOC chemistry than in the remote atmosphere. [A higher  
725 resolution TCOH product over land would also likely be feasible, because of the increased signal to noise  
726 of the NO<sub>2</sub> and HCHO retrievals.](#) Expanding this product beyond the tropics could increase  
727 understanding of global CH<sub>4</sub>, CO, and VOC trends and variability and allow for a wider range of satellite  
728 retrievals as inputs. For example, current and upcoming geostationary air quality satellites such as

729 Sentinel 4, TEMPO (Tropospheric Emissions: Monitoring of Pollution), and GEMS (Geostationary  
730 Environment Monitoring Spectrometer) could provide retrievals of most of the necessary inputs to the  
731 machine learning model, allowing for the understanding of diurnal variability in TCOH and potentially in  
732 the diurnal variability of ozone production (Zhu et al., 2022a).

733  
734 A similar methodology could likely be used to determine OH at different layers of the atmosphere.  
735 Because CH<sub>4</sub> loss is not evenly distributed throughout the tropospheric column, vertically resolved OH  
736 would better help inform this process. Vertically-resolved OH could also help understand differences in  
737 OH drivers in the upper and lower troposphere (Spivakovsky et al., 1990;Lelieveld et al., 2016), which  
738 can often be decoupled from the column. While column inputs, such as those discussed here, could be  
739 used, the inclusion of vertically resolved satellite retrievals, such as the AIRS H<sub>2</sub>O<sub>(v)</sub> layers, would provide  
740 additional information. Tropospheric O<sub>3</sub> at different atmospheric layers, such as that previously  
741 provided by the TES satellite, could also be invaluable here, as O<sub>3</sub> is a large driver of primary OH  
742 production.

743  
744 Satellite-derived OH would also provide a much-needed, observational constraint on OH variability in  
745 global chemistry models. Because the methodology can capture variability in TCOH of both  
746 observations and 3-dimensional model output, TCOH trends from a satellite-constrained product could  
747 be used to evaluate modeled trends and as well as the spatial variability resulting from events like ENSO.  
748 While the satellite-derived OH could not explicitly indicate the cause of differences, the spatial  
749 distribution of the differences as well as differences in observed and modeled machine learning model  
750 inputs could indicate potential dynamical or emission sources of error in the 3D model.

751  
752 Further, the combination of the satellite-derived OH and the machine learning model could help identify  
753 the impacts of any diagnosed errors in emissions inventories as well as the impacts of unexpected  
754 events, such as COVID-19-related shutdowns, on TCOH. For example, if there are significant  
755 discrepancies between observed and modeled NO<sub>2</sub> in a specific region of the atmosphere, the satellite  
756 NO<sub>2</sub> could be scaled to more closely match the 3D model values and then be input into the machine  
757 learning model. The difference in TCOH would then indicate the relative impact of the model error. This  
758 would serve as a computationally efficient complement to other methodologies constraining models  
759 with observations (e.g. Miyazaki et al., 2020;Miyazaki et al., 2021) to identify the impacts of these errors  
760 on the atmospheric oxidation capacity. A similar methodology could be used for unexpected events that  
761 significantly impact emissions of OH drivers, allowing for quick determination of their potential impacts  
762 on the atmospheric oxidation capacity before emissions inventories could be revised.

763  
764 While we have shown that the methodology captures the variability of observed OH and generally  
765 agrees with observations within measurement uncertainty, it is unclear whether differences result from  
766 GBRT model deficiencies or structural differences between the *in situ* observations and the training  
767 dataset. Additional field campaigns with observations of OH and the GBRT model inputs would allow for  
768 a more thorough evaluation of both the OH product and the methodology itself. Such a field campaign  
769 would need to provide complete tropospheric columns of all species and cover less horizontal distance  
770 than the ATom profiles (e.g. from spiral flight patterns). In situ observations of NO<sub>2</sub> without significant  
771 interference from NO<sub>x</sub> reservoir species are also needed to reduce uncertainty. Alternatively, NO<sub>2</sub> and  
772 other species could be measured through aircraft-based remote sensing. Finally, repeated sampling over  
773 the same locations for multiple days within a defined area would allow for meaningful statistical analysis  
774 while also allowing for the comparison of TCOH columns calculated from satellite observations.

775

776 Finally, accuracy of the TCOH product is dependent on the accuracy of the satellite retrievals input into  
777 the machine learning model, with the NO<sub>2</sub> retrieval having the largest effect. To reduce the uncertainty  
778 of the TCOH product, more information about the accuracy of individual NO<sub>2</sub> retrievals is required.  
779 Currently, there is little validation of OMI and TROPOMI NO<sub>2</sub> retrievals in the remote, tropical  
780 atmosphere, so it is difficult to assess which retrievals, if any, are correct. Recent efforts, such as the  
781 QA4ECV (Quality Assurance for the Essential Climate Variables), to improve NO<sub>2</sub> retrieval algorithms  
782 have reduced uncertainty, particularly over land (Boersma et al., 2018), although it is unclear how the  
783 accuracy of these retrievals translates to the remote tropics as validation data are still extremely limited.  
784 Even retrievals of TROPOMI and OMI made with the same algorithm show differences, suggesting that  
785 instrumental differences could also affect the results. Future satellite missions should focus on trying to  
786 reduce the uncertainty in NO<sub>2</sub> retrievals, particularly in the remote atmosphere, both through  
787 improvements in instrument design and algorithm development.  
788

## 789 **7 Data Availability**

790 Output from the MERRA2 GMI simulation are publicly available at [https://acd-  
791 ext.gsfc.nasa.gov/Projects/GEOSCCM/MERRA2GMI/](https://acd-ext.gsfc.nasa.gov/Projects/GEOSCCM/MERRA2GMI/) (NASA Goddard Space Flight Center, 2023). All  
792 satellite products, except for TROPOMI water vapor, are available at <https://disc.gsfc.nasa.gov> (GES  
793 DISC, 2023). Data from the ATom campaign are located at <https://daac.ornl.gov> (Wofsy et al., 2021).  
794

## 795 **8 Author contributions**

796 DCA wrote the manuscript, performed the data analysis, and created the GBRT model. DCA, BND, JMN,  
797 and MBFC developed the idea for the methodology. SAS performed three-dimensional modeling for the  
798 work. JMN provided advice on machine learning. JL helped perform data analysis. All authors helped  
799 develop ideas for the analysis and contributed to the manuscript.  
800

## 801 **9 Competing Interests**

802 BND is a member of the editorial board of Atmospheric Chemistry and Physics. The peer-review process  
803 was guided by an independent editor, and the authors also have no other competing interests to  
804 declare.  
805

## 806 **10 Financial support**

807 This research has been supported by the National Aeronautics and Space Administration (NASA)  
808 Atmospheric Composition Campaign Data Analysis and Modeling (ACCDAM) program (grant no.  
809 80NSSC21K1440).  
810

## 811 **11 Acknowledgements**

812 The authors wish to thank Lok Chan and Diego Loyola for use of the TROPOMI water vapor product.  
813

## 814 **10. References**

815  
816 Anderson, D. C., Nicely, J. M., Salawitch, R. J., Canty, T. P., Dickerson, R. R., Hanisco, T. F., Wolfe, G. M.,  
817 Apel, E. C., Atlas, E., Bannan, T., Bauguitte, S., Blake, N. J., Bresch, J. F., Campos, T. L., Carpenter, L. J.,  
818 Cohen, M. D., Evans, M., Fernandez, R. P., Kahn, B. H., Kinnison, D. E., Hall, S. R., Harris, N. R., Hornbrook,  
819 R. S., Lamarque, J. F., Le Breton, M., Lee, J. D., Percival, C., Pfister, L., Pierce, R. B., Riemer, D. D., Saiz-  
820 Lopez, A., Stunder, B. J., Thompson, A. M., Ullmann, K., Vaughan, A., and Weinheimer, A. J.: A pervasive  
821 role for biomass burning in tropical high ozone/low water structures, *Nat Commun*, 7, 10267,  
822 10.1038/ncomms10267, 2016.

823 Anderson, D. C., Duncan, B. N., Fiore, A. M., Baublitz, C. B., Follette-Cook, M. B., Nicely, J. M., and Wolfe,  
824 G. M.: Spatial and temporal variability in the hydroxyl (OH) radical: understanding the role of large-scale  
825 climate features and their influence on OH through its dynamical and photochemical drivers,  
826 *Atmospheric Chemistry and Physics*, 21, 6481-6508, 10.5194/acp-21-6481-2021, 2021.

827 Anderson, D. C., Follette-Cook, M. B., Strode, S. A., Nicely, J. M., Liu, J., Ivatt, P. D., and Duncan, B. N.: A  
828 machine learning methodology for the generation of a parameterization of the hydroxyl radical, *Geosci.*  
829 *Model Dev.*, 15, 6341-6358, 10.5194/gmd-15-6341-2022, 2022.

830 Bedka, S., Knuteson, R., Revercomb, H., Tobin, D., and Turner, D.: An assessment of the absolute  
831 accuracy of the Atmospheric Infrared Sounder v5 precipitable water vapor product at tropical,  
832 midlatitude, and arctic ground-truth sites: September 2002 through August 2008, *Journal of Geophysical*  
833 *Research: Atmospheres*, 115, D17310, <https://doi.org/10.1029/2009JD013139>, 2010.

834 Boersma, K. F., Eskes, H. J., Richter, A., De Smedt, I., Lorente, A., Beirle, S., van Geffen, J. H. G. M., Zara,  
835 M., Peters, E., Van Roozendaal, M., Wagner, T., Maasakkers, J. D., van der A, R. J., Nightingale, J., De  
836 Rudder, A., Irie, H., Pinardi, G., Lambert, J. C., and Compernelle, S. C.: Improving algorithms and  
837 uncertainty estimates for satellite NO<sub>2</sub> retrievals: results from the quality assurance for the essential  
838 climate variables (QA4ECV) project, *Atmos. Meas. Tech.*, 11, 6651-6678, 10.5194/amt-11-6651-2018,  
839 2018.

840 Borsdorff, T., aan de Brugh, J., Schneider, A., Lorente, A., Birk, M., Wagner, G., Kivi, R., Hase, F., Feist, D.  
841 G., Sussmann, R., Rettinger, M., Wunch, D., Warneke, T., and Landgraf, J.: Improving the TROPOMI CO  
842 data product: update of the spectroscopic database and destriping of single orbits, *Atmos. Meas. Tech.*,  
843 12, 5443-5455, 10.5194/amt-12-5443-2019, 2019.

844 Brune, W. H., Miller, D. O., Thames, A. B., Allen, H. M., Apel, E. C., Blake, D. R., Bui, T. P., Commane, R.,  
845 Crouse, J. D., Daube, B. C., Diskin, G. S., DiGangi, J. P., Elkins, J. W., Hall, S. R., Hanisco, T. F., Hannun, R.  
846 A., Hintsa, E. J., Hornbrook, R. S., Kim, M. J., McKain, K., Moore, F. L., Neuman, J. A., Nicely, J. M., Peischl,  
847 J., Ryerson, T. B., St. Clair, J. M., Sweeney, C., Teng, A. P., Thompson, C., Ullmann, K., Veres, P. R.,  
848 Wennberg, P. O., and Wolfe, G. M.: Exploring Oxidation in the Remote Free Troposphere: Insights From  
849 Atmospheric Tomography (ATom), *Journal of Geophysical Research: Atmospheres*, 125, e1019JD031685,  
850 10.1029/2019jd031685, 2020.

851 Buchholz, R. R., Deeter, M. N., Worden, H. M., Gille, J., Edwards, D. P., Hannigan, J. W., Jones, N. B.,  
852 Paton-Walsh, C., Griffith, D. W. T., Smale, D., Robinson, J., Strong, K., Conway, S., Sussmann, R., Hase, F.,  
853 Blumenstock, T., Mahieu, E., and Langerock, B.: Validation of MOPITT carbon monoxide using ground-  
854 based Fourier transform infrared spectrometer data from NDACC, *Atmos. Meas. Tech.*, 10, 1927-1956,  
855 10.5194/amt-10-1927-2017, 2017.

856 Burnett, C. R., and Minschwaner, K.: Continuing development in the regime of decreased atmospheric  
857 column OH at Fritz Peak, Colorado, *Geophysical Research Letters*, 25, 1313-1316,  
858 <https://doi.org/10.1029/98GL01062>, 1998.

859 Chan, K. L., Xu, J., Slijkhuis, S., Valks, P., and Loyola, D.: TROPOspheric Monitoring Instrument  
860 observations of total column water vapour: Algorithm and validation, *Science of The Total Environment*,  
861 821, 153232, <https://doi.org/10.1016/j.scitotenv.2022.153232>, 2022.

862 Chen, T., and Guestrin, C.: XGBoost: A Scalable Tree Boosting System, KDD '16: Proceedings of the 22nd  
863 ACM SIGKDD International Conference on Knowledge Discovery and Data Mining, 13 - 17 Aug. 2016,  
864 785-794, San Francisco, CA, USA, <https://doi.org/10.1145/2939672.2939785>, 2016.

865 Chin, T. M., Vazquez-Cuervo, J., and Armstrong, E. M.: A multi-scale high-resolution analysis of global sea  
866 surface temperature, *Remote Sensing of Environment*, 200, 154-169,  
867 <https://doi.org/10.1016/j.rse.2017.07.029>, 2017.

868 Choi, S., Lamsal, L. N., Follette-Cook, M., Joiner, J., Krotkov, N. A., Swartz, W. H., Pickering, K. E.,  
869 Loughner, C. P., Appel, W., Pfister, G., Saide, P. E., Cohen, R. C., Weinheimer, A. J., and Herman, J. R.:  
870 Assessment of NO<sub>2</sub> observations during DISCOVER-AQ and KORUS-AQ field campaigns, *Atmos. Meas.*  
871 *Tech.*, 13, 2523-2546, 10.5194/amt-13-2523-2020, 2020.

872 De Smedt, I., Theys, N., Yu, H., Danckaert, T., Lerot, C., Compernelle, S., Van Roozendaal, M., Richter, A.,  
873 Hilboll, A., Peters, E., Pedernana, M., Loyola, D., Beirle, S., Wagner, T., Eskes, H., van Geffen, J.,  
874 Boersma, K. F., and Veefkind, P.: Algorithm theoretical baseline for formaldehyde retrievals from S5P  
875 TROPOMI and from the QA4ECV project, *Atmospheric Measurement Techniques*, 11, 2395-2426,  
876 10.5194/amt-11-2395-2018, 2018.

877 De Smedt, I., Pinardi, G., Vigouroux, C., Compernelle, S., Bais, A., Benavent, N., Boersma, F., Chan, K. L.,  
878 Donner, S., Eichmann, K. U., Hedelt, P., Hendrick, F., Irie, H., Kumar, V., Lambert, J. C., Langerock, B.,  
879 Lerot, C., Liu, C., Loyola, D., Piters, A., Richter, A., Rivera Cárdenas, C., Romahn, F., Ryan, R. G., Sinha, V.,  
880 Theys, N., Vlietinck, J., Wagner, T., Wang, T., Yu, H., and Van Roozendaal, M.: Comparative assessment  
881 of TROPOMI and OMI formaldehyde observations and validation against MAX-DOAS network column  
882 measurements, *Atmos. Chem. Phys.*, 21, 12561-12593, 10.5194/acp-21-12561-2021, 2021.

883 Deeter, M. N., Edwards, D. P., Francis, G. L., Gille, J. C., Mao, D., Martínez-Alonso, S., Worden, H. M.,  
884 Ziskin, D., and Andreae, M. O.: Radiance-based retrieval bias mitigation for the MOPITT instrument: the  
885 version 8 product, *Atmospheric Measurement Techniques*, 12, 4561-4580, 10.5194/amt-12-4561-2019,  
886 2019.

887 Duncan, B., Portman, D., Bey, I., and Spivakovsky, C.: Parameterization of OH for efficient computation in  
888 chemical tracer models, *Journal of Geophysical Research: Atmospheres*, 105, 12259-12262,  
889 10.1029/1999JD901141, 2000.

890 Duncan, B. N., Strahan, S. E., Yoshida, Y., Steenrod, S. D., and Livesey, N.: Model study of the cross-  
891 tropopause transport of biomass burning pollution, *Atmos. Chem. Phys.*, 7, 3713-3736, 10.5194/acp-7-  
892 3713-2007, 2007.

893 Elith, J., Leathwick, J. R., and Hastie, T.: A working guide to boosted regression trees, *J Anim Ecol*, 77,  
894 802-813, 10.1111/j.1365-2656.2008.01390.x, 2008.

895 Garane, K., Koukouli, M. E., Verhoelst, T., Lerot, C., Heue, K. P., Fioletov, V., Balis, D., Bais, A., Bazureau,  
896 A., Dehn, A., Goutail, F., Granville, J., Griffin, D., Hubert, D., Keppens, A., Lambert, J. C., Loyola, D.,  
897 McLinden, C., Pazmino, A., Pommereau, J. P., Redondas, A., Romahn, F., Valks, P., Van Roozendaal, M.,  
898 Xu, J., Zehner, C., Zerefos, C., and Zimmer, W.: TROPOMI/S5P total ozone column data: global ground-  
899 based validation and consistency with other satellite missions, *Atmos. Meas. Tech.*, 12, 5263-5287,  
900 10.5194/amt-12-5263-2019, 2019.



901 Gelaro, R., McCarty, W., Suarez, M. J., Todling, R., Molod, A., Takacs, L., Randles, C., Darmenov, A.,  
902 Bosilovich, M. G., Reichle, R., Wargan, K., Coy, L., Cullather, R., Draper, C., Akella, S., Buchard, V., Conaty,  
903 A., da Silva, A., Gu, W., Kim, G. K., Koster, R., Lucchesi, R., Merkova, D., Nielsen, J. E., Partyka, G.,  
904 Pawson, S., Putman, W., Rienecker, M., Schubert, S. D., Sienkiewicz, M., and Zhao, B.: The Modern-Era  
905 Retrospective Analysis for Research and Applications, Version 2 (MERRA-2), *J Clim*, Volume 30, 5419-  
906 5454, 10.1175/JCLI-D-16-0758.1, 2017.

907 GES DISC: Earth Science Data at NASA, available at <https://disc.gsfc.nasa.gov>, last access: 6 Mar. 2023.

908 González Abad, G., Liu, X., Chance, K., Wang, H., Kurosu, T. P., and Suleiman, R.: Updated Smithsonian  
909 Astrophysical Observatory Ozone Monitoring Instrument (SAO OMI) formaldehyde retrieval,  
910 *Atmospheric Measurement Techniques*, 8, 19-32, 10.5194/amt-8-19-2015, 2015.

911 González Abad, G., Vasilkov, A., Seftor, C., Liu, X., and Chance, K.: Smithsonian Astrophysical Observatory  
912 Ozone Mapping and Profiler Suite (SAO OMPS) formaldehyde retrieval, *Atmospheric Measurement*  
913 *Techniques*, 9, 2797-2812, 10.5194/amt-9-2797-2016, 2016.

914 Hedelius, J. K., He, T. L., Jones, D. B. A., Baier, B. C., Buchholz, R. R., De Mazière, M., Deutscher, N. M.,  
915 Dubey, M. K., Feist, D. G., Griffith, D. W. T., Hase, F., Iraci, L. T., Jeseck, P., Kiel, M., Kivi, R., Liu, C.,  
916 Morino, I., Notholt, J., Oh, Y. S., Ohyama, H., Pollard, D. F., Rettinger, M., Roche, S., Roehl, C. M.,  
917 Schneider, M., Shiomi, K., Strong, K., Sussmann, R., Sweeney, C., Té, Y., Uchino, O., Velazco, V. A., Wang,  
918 W., Warneke, T., Wennberg, P. O., Worden, H. M., and Wunch, D.: Evaluation of MOPITT Version 7 joint  
919 TIR–NIR XCO retrievals with TCCON, *Atmos. Meas. Tech.*, 12, 5547-5572, 10.5194/amt-12-5547-2019,  
920 2019.

921 Ivatt, P. D., and Evans, M. J.: Improving the prediction of an atmospheric chemistry transport model  
922 using gradient-boosted regression trees, *Atmospheric Chemistry and Physics*, 20, 8063-8082,  
923 10.5194/acp-20-8063-2020, 2020.

924 Keller, C. A., and Evans, M. J.: Application of random forest regression to the calculation of gas-phase  
925 chemistry within the GEOS-Chem chemistry model v10, *Geoscientific Model Development*, 12, 1209-  
926 1225, 10.5194/gmd-12-1209-2019, 2019.

927 Kelp, M. M., Jacob, D. J., Kutz, J. N., Marshall, J. D., and Tessum, C. W.: Toward Stable, General Machine-  
928 Learned Models of the Atmospheric Chemical System, *Journal of Geophysical Research: Atmospheres*,  
929 125, e2020JD032759, <https://doi.org/10.1029/2020JD032759>, 2020.

930 Labow, G. J., McPeters, R. D., Bhartia, P. K., and Kramarova, N.: A comparison of 40 years of SBUV  
931 measurements of column ozone with data from the Dobson/Brewer network, *Journal of Geophysical*  
932 *Research: Atmospheres*, 118, 7370-7378, <https://doi.org/10.1002/jgrd.50503>, 2013.

933 Lamsal, L. N., Krotkov, N. A., Celarier, E. A., Swartz, W. H., Pickering, K. E., Bucsela, E. J., Gleason, J. F.,  
934 Martin, R. V., Philip, S., Irie, H., Cede, A., Herman, J., Weinheimer, A., Szykman, J. J., and Knepp, T. N.:  
935 Evaluation of OMI operational standard NO<sub>2</sub> column retrievals using in situ and surface-based NO<sub>2</sub>  
936 observations, *Atmospheric Chemistry and Physics*, 14, 11587-11609, 10.5194/acp-14-11587-2014, 2014.

937 Lamsal, L. N., Krotkov, N. A., Vasilkov, A., Marchenko, S., Qin, W., Yang, E. S., Fasnacht, Z., Joiner, J., Choi,  
938 S., Haffner, D., Swartz, W. H., Fisher, B., and Bucsela, E.: Ozone Monitoring Instrument (OMI) Aura

939 nitrogen dioxide standard product version 4.0 with improved surface and cloud treatments, *Atmos.*  
940 *Meas. Tech.*, 14, 455-479, 10.5194/amt-14-455-2021, 2021.

941 Lamsal, L. N., Krotkov, N. A., Marchenko, S. V., Joiner, J., Oman, L., Vasilkov, A., Fisher, B., Qin, W., Yang,  
942 E.-S., Fasnacht, Z., Choi, S., Leonard, P., and Haffner, D.: TROPOMI/S5P NO<sub>2</sub> Tropospheric, Stratospheric  
943 and Total Columns MINDS 1-Orbit L2 Swath 5.5 km x 3.5 km, in, NASA Goddard Earth Sciences Data and  
944 Information Services Center (GES DISC) [data set], <https://10.5067/MEASURES/MINDS/Data203>, 2022.

945 Laughner, J. L., Neu, J. L., Schimel, D., Wennberg, P. O., Barsanti, K., Bowman, K. W., Chatterjee, A.,  
946 Croes, B. E., Fitzmaurice, H. L., Henze, D. K., Kim, J., Kort, E. A., Liu, Z., Miyazaki, K., Turner, A. J.,  
947 Anenberg, S., Avise, J., Cao, H., Crisp, D., de Gouw, J., Eldering, A., Fyfe, J. C., Goldberg, D. L., Gurney, K.  
948 R., Hasheminassab, S., Hopkins, F., Ivey, C. E., Jones, D. B. A., Liu, J., Lovenduski, N. S., Martin, R. V.,  
949 McKinley, G. A., Ott, L., Poulter, B., Ru, M., Sander, S. P., Swart, N., Yung, Y. L., and Zeng, Z. C.: Societal  
950 shifts due to COVID-19 reveal large-scale complexities and feedbacks between atmospheric chemistry  
951 and climate change, *Proc Natl Acad Sci U S A*, 118, e2109481118, 10.1073/pnas.2109481118, 2021.

952 Lelieveld, J., Gromov, S., Pozzer, A., and Taraborrelli, D.: Global tropospheric hydroxyl distribution,  
953 budget and reactivity, *Atmos. Chem. Phys.*, 16, 12477-12493, 10.5194/acp-16-12477-2016, 2016.

954 Levy, R. C., Mattoo, S., Munchak, L. A., Remer, L. A., Sayer, A. M., Patadia, F., and Hsu, N. C.: The  
955 Collection 6 MODIS aerosol products over land and ocean, *Atmos. Meas. Tech.*, 6, 2989-3034,  
956 10.5194/amt-6-2989-2013, 2013.

957 Liang, Q., Chipperfield, M. P., Fleming, E. L., Abraham, N. L., Braesicke, P., Burkholder, J. B., Daniel, J. S.,  
958 Dhomse, S., Fraser, P. J., Hardiman, S. C., Jackman, C. H., Kinnison, D. E., Krummel, P. B., Montzka, S. A.,  
959 Morgenstern, O., McCulloch, A., Mühle, J., Newman, P. A., Orkin, V. L., Pitari, G., Prinn, R. G., Rigby, M.,  
960 Rozanov, E., Stenke, A., Tummon, F., Velders, G. J. M., Visioni, D., and Weiss, R. F.: Deriving Global OH  
961 Abundance and Atmospheric Lifetimes for Long-Lived Gases: A Search for CH<sub>3</sub>CCl<sub>3</sub> Alternatives, *Journal*  
962 *of Geophysical Research: Atmospheres*, 122, 11,914-911,933, 10.1002/2017JD026926, 2017.

963 Lovelock, J. E.: Methyl chloroform in the troposphere as an indicator of OH radical abundance, *Nature*,  
964 267, 32-32, 10.1038/267032a0, 1977.

965 Mao, J., Ren, X., Brune, W. H., Olson, J. R., Crawford, J. H., Fried, A., Huey, L. G., Cohen, R. C., Heikes, B.,  
966 Singh, H. B., Blake, D. R., Sachse, G. W., Diskin, G. S., Hall, S. R., and Shetter, R. E.: Airborne measurement  
967 of OH reactivity during INTEX-B, *Atmos. Chem. Phys.*, 9, 163-173, 10.5194/acp-9-163-2009, 2009.

968 Martínez-Alonso, S., Deeter, M., Worden, H., Borsdorff, T., Aben, I., Commane, R., Daube, B., Francis, G.,  
969 George, M., Landgraf, J., Mao, D., McKain, K., and Wofsy, S.: 1.5 years of TROPOMI CO measurements:  
970 comparisons to MOPITT and ATom, *Atmos. Meas. Tech.*, 13, 4841-4864, 10.5194/amt-13-4841-2020,  
971 2020.

972 McPeters, R. D., Frith, S., and Labow, G. J.: OMI total column ozone: extending the long-term data  
973 record, *Atmos. Meas. Tech.*, 8, 4845-4850, 10.5194/amt-8-4845-2015, 2015.

974 Miller, D. O., and Brune, W. H.: Investigating the Understanding of Oxidation Chemistry Using 20 Years  
975 of Airborne OH and HO<sub>2</sub> Observations, *Journal of Geophysical Research: Atmospheres*, 127,  
976 e2021JD035368, <https://doi.org/10.1029/2021JD035368>, 2022.



977 Miyazaki, K., Bowman, K. W., Yumimoto, K., Walker, T., and Sudo, K.: Evaluation of a multi-model, multi-  
978 constituent assimilation framework for tropospheric chemical reanalysis, *Atmos. Chem. Phys.*, 20, 931-  
979 967, 10.5194/acp-20-931-2020, 2020.

980 Miyazaki, K., Bowman, K., Sekiya, T., Takigawa, M., Neu, J. L., Sudo, K., Osterman, G., and Eskes, H.:  
981 Global tropospheric ozone responses to reduced NO<sub>x</sub> emissions linked to the COVID-19 worldwide  
982 lockdowns, *Science Advances*, 7, eabf7460, 10.1126/sciadv.abf7460, 2021.

983 Montzka, S. A., Krol, M., Dlugokencky, E., Hall, B., Jockel, P., and Lelieveld, J.: Small Interannual  
984 Variability of Global Atmospheric Hydroxyl, *Science*, 331, 67-69, 10.1126/science.1197640, 2011.

985 Murray, L. T., Mickley, L. J., Kaplan, J. O., Sofen, E. D., Pfeiffer, M., and Alexander, B.: Factors controlling  
986 variability in the oxidative capacity of the troposphere since the Last Glacial Maximum, *Atmospheric*  
987 *Chemistry and Physics*, 14, 3589-3622, 10.5194/acp-14-3589-2014, 2014.

988 Murray, L. T., Fiore, A. M., Shindell, D. T., Naik, V., and Horowitz, L. W.: Large uncertainties in global  
989 hydroxyl projections tied to fate of reactive nitrogen and carbon, *Proceedings of the National Academy*  
990 *of Sciences*, 118, e2115204118, 10.1073/pnas.2115204118, 2021.

991 NASA Goddard Space Flight Center. MERRA2 GMI, NASA [data set], [https://acd-  
992 ext.gsfc.nasa.gov/Projects/GEOSCCM/MERRA2GMI/](https://acd-ext.gsfc.nasa.gov/Projects/GEOSCCM/MERRA2GMI/), last access: 6 March 2023.

993 Nault, B. A., Garland, C., Pusede, S. E., Wooldridge, P. J., Ullmann, K., Hall, S. R., and Cohen, R. C.:  
994 Measurements of CH<sub>3</sub>O<sub>2</sub>NO<sub>2</sub> in the upper troposphere, *Atmospheric Measurement Techniques*, 8, 987-  
995 997, 10.5194/amt-8-987-2015, 2015.

996 Naus, S., Montzka, S. A., Pandey, S., Basu, S., Dlugokencky, E. J., and Krol, M.: Constraints and biases in a  
997 tropospheric two-box model of OH, *Atmos. Chem. Phys.*, 19, 407-424, 10.5194/acp-19-407-2019, 2019.

998 Naus, S., Montzka, S. A., Patra, P. K., and Krol, M. C.: A three-dimensional-model inversion of methyl  
999 chloroform to constrain the atmospheric oxidative capacity, *Atmospheric Chemistry and Physics*, 21,  
1000 4809-4824, 10.5194/acp-21-4809-2021, 2021.

1001 Nicely, J. M., Salawitch, R. J., Canty, T., Anderson, D. C., Arnold, S. R., Chipperfield, M. P., Emmons, L. K.,  
1002 Flemming, J., Huijnen, V., Kinnison, D. E., Lamarque, J.-F., Mao, J., Monks, S. A., Steenrod, S. D., Tilmes,  
1003 S., and Turquety, S.: Quantifying the causes of differences in tropospheric OH within global models,  
1004 *Journal of Geophysical Research: Atmospheres*, JD026239, 10.1002/2016JD026239, 2017.

1005 Nicely, J. M., Duncan, B. N., Hanisco, T. F., Wolfe, G. M., Salawitch, R. J., Deushi, M., Haslerud, A. S.,  
1006 Jöckel, P., Josse, B., Kinnison, D. E., Klekociuk, A., Manyin, M. E., Marécal, V., Morgenstern, O., Murray, L.  
1007 T., Myhre, G., Oman, L. D., Pitari, G., Pozzer, A., Quaglia, I., Revell, L. E., Rozanov, E., Stenke, A., Stone, K.,  
1008 Strahan, S., Tilmes, S., Tost, H., Westervelt, D. M., and Zeng, G.: A machine learning examination of  
1009 hydroxyl radical differences among model simulations for CCMI-1, *Atmospheric Chemistry and Physics*,  
1010 20, 1341-1361, 10.5194/acp-20-1341-2020, 2020.

1011 Oman, L. D., Douglass, A. R., Ziemke, J. R., Rodriguez, J. M., Waugh, D. W., and Nielsen, J. E.: The ozone  
1012 response to ENSO in Aura satellite measurements and a chemistry-climate simulation, *Journal of*  
1013 *Geophysical Research-Atmospheres*, 118, 965-976, 10.1029/2012jd018546, 2013.

- 1014 Orbe, C., Oman, L. D., Strahan, S. E., Waugh, D. W., Pawson, S., Takacs, L. L., and Molod, A. M.: Large-  
1015 Scale Atmospheric Transport in GEOS Replay Simulations, *Journal of Advances in Modeling Earth*  
1016 *Systems*, 9, 2545-2560, [10.1002/2017ms001053](https://doi.org/10.1002/2017ms001053), 2017.
- 1017 Patra, P. K., Krol, M. C., Montzka, S. A., Arnold, T., Atlas, E. L., Lintner, B. R., Stephens, B. B., Xiang, B.,  
1018 Elkins, J. W., Fraser, P. J., Ghosh, A., Hints, E. J., Hurst, D. F., Ishijima, K., Krummel, P. B., Miller, B. R.,  
1019 Miyazaki, K., Moore, F. L., Muhle, J., O'Doherty, S., Prinn, R. G., Steele, L. P., Takigawa, M., Wang, H. J.,  
1020 Weiss, R. F., Wofsy, S. C., and Young, D.: Observational evidence for interhemispheric hydroxyl-radical  
1021 parity, *Nature*, 513, 219-223, [10.1038/nature13721](https://doi.org/10.1038/nature13721), 2014.
- 1022 Pérez-Ramírez, D., Smirnov, A., Pinker, R. T., Petrenko, M., Román, R., Chen, W., Ichoku, C., Noël, S.,  
1023 Abad, G. G., Lyamani, H., and Holben, B. N.: Precipitable water vapor over oceans from the Maritime  
1024 Aerosol Network: Evaluation of global models and satellite products under clear sky conditions,  
1025 *Atmospheric Research*, 215, 294-304, <https://doi.org/10.1016/j.atmosres.2018.09.007>, 2019.
- 1026 Pickett, H. M., Drouin, B. J., Canty, T., Salawitch, R. J., Fuller, R. A., Perun, V. S., Livesey, N. J., Waters, J.  
1027 W., Stachnik, R. A., Sander, S. P., Traub, W. A., Jucks, K. W., and Minschwaner, K.: Validation of Aura  
1028 Microwave Limb Sounder OH and HO<sub>2</sub> measurements, *Journal of Geophysical Research: Atmospheres*,  
1029 113, D16S30, <https://doi.org/10.1029/2007JD008775>, 2008.
- 1030 Pimlott, M. A., Pope, R. J., Kerridge, B. J., Latter, B. G., Knappett, D. S., Heard, D. E., Ventress, L. J.,  
1031 Siddans, R., Feng, W., and Chipperfield, M. P.: Investigating the global OH radical distribution using  
1032 steady-state approximations and satellite data, *Atmos. Chem. Phys.*, 22, 10467-10488, [10.5194/acp-22-](https://doi.org/10.5194/acp-22-10467-2022)  
1033 [10467-2022](https://doi.org/10.5194/acp-22-10467-2022), 2022.
- 1034 Rigby, M., Montzka, S. A., Prinn, R. G., White, J. W. C., Young, D., O'Doherty, S., Lunt, M. F., Ganesan, A.  
1035 L., Manning, A. J., Simmonds, P. G., Salameh, P. K., Harth, C. M., Muhle, J., Weiss, R. F., Fraser, P. J.,  
1036 Steele, L. P., Krummel, P. B., McCulloch, A., and Park, S.: Role of atmospheric oxidation in recent  
1037 methane growth, *Proc Natl Acad Sci U S A*, 114, 5373-5377, [10.1073/pnas.1616426114](https://doi.org/10.1073/pnas.1616426114), 2017.
- 1038 Shah, V., Jacob, D. J., Dang, R., Lamsal, L. N., Strode, S. A., Steenrod, S. D., Boersma, K. F., Eastham, S. D.,  
1039 Fritz, T. M., Thompson, C., Peischl, J., Bourgeois, I., Pollack, I. B., Nault, B. A., Cohen, R. C., Campuzano-  
1040 Jost, P., Jimenez, J. L., Andersen, S. T., Carpenter, L. J., Sherwen, T., and Evans, M. J.: Nitrogen oxides in  
1041 the free troposphere: implications for tropospheric oxidants and the interpretation of satellite NO<sub>2</sub>  
1042 measurements, *Atmos. Chem. Phys.*, 23, 1227-1257, [10.5194/acp-23-1227-2023](https://doi.org/10.5194/acp-23-1227-2023), 2023.
- 1043 Silvern, R. F., Jacob, D. J., Travis, K. R., Sherwen, T., Evans, M. J., Cohen, R. C., Laughner, J. L., Hall, S. R.,  
1044 Ullmann, K., Crounse, J. D., Wennberg, P. O., Peischl, J., and Pollack, I. B.: Observed NO/NO<sub>2</sub> Ratios in  
1045 the Upper Troposphere Imply Errors in NO-NO<sub>2</sub>-O<sub>3</sub> Cycling Kinetics or an Unaccounted NO<sub>x</sub> Reservoir,  
1046 *Geophysical Research Letters*, 45, 4466-4474, <https://doi.org/10.1029/2018GL077728>, 2018.
- 1047 [Spivakovsky, C. M., Logan, J. A., Montzka, S. A., Balkanski, Y. J., Foreman-Fowler, M., Jones, D. B. A.,](https://doi.org/10.1029/1999jd901006)  
1048 [Horowitz, L. W., Fusco, A. C., Brenninkmeijer, C. A. M., Prather, M. J., Wofsy, S. C., and McElroy, M. B.:](https://doi.org/10.1029/1999jd901006)  
1049 [Three-dimensional climatological distribution of tropospheric OH: Update and evaluation, \*Journal of\*](https://doi.org/10.1029/1999jd901006)  
1050 [\*Geophysical Research: Atmospheres\*, 105, 8931-8980, 10.1029/1999jd901006, 2000.](https://doi.org/10.1029/1999jd901006)
- 1051 Stauffer, R. M., Thompson, A. M., and Young, G. S.: Tropospheric ozonesonde profiles at long-term U.S.  
1052 monitoring sites: 1. A climatology based on self-organizing maps, *Journal of Geophysical Research:*  
1053 *Atmospheres*, 121, 1320-1339, <https://doi.org/10.1002/2015JD023641>, 2016.

1054 Stevenson, D. S., Zhao, A., Naik, V., amp, apos, Connor, F. M., Tilmes, S., Zeng, G., Murray, L. T., Collins,  
1055 W. J., Griffiths, P., Shim, S., Horowitz, L. W., Sentman, L., and Emmons, L.: Trends in global tropospheric  
1056 hydroxyl radical and methane lifetime since 1850 from AerChemMIP, *Atmos. Chem. Phys.*, 20, 12905-  
1057 12920, <https://doi.org/10.5194/acp-20-12905-2020>, 2020.

1058  
1059 Strahan, S. E., Duncan, B. N., and Hoor, P.: Observationally derived transport diagnostics for the  
1060 lowermost stratosphere and their application to the GMI chemistry and transport model, *Atmos. Chem.*  
1061 *Phys.*, 7, 2435-2445, [10.5194/acp-7-2435-2007](https://doi.org/10.5194/acp-7-2435-2007), 2007.

1062  
1063 Strode, S. A., Ziemke, J. R., Oman, L. D., Lamsal, L. N., Olsen, M. A., and Liu, J.: Global changes in the  
1064 diurnal cycle of surface ozone, *Atmospheric Environment*, 199, 323-333,  
[10.1016/j.atmosenv.2018.11.028](https://doi.org/10.1016/j.atmosenv.2018.11.028), 2019.

1065  
1066 Susskind, J., Blaisdell, J. M., and Iredell, L.: Improved methodology for surface and atmospheric  
1067 soundings, error estimates, and quality control procedures: the atmospheric infrared sounder science  
1068 team version-6 retrieval algorithm, *Journal of Applied Remote Sensing*, 8, 084994,  
[10.1117/1.Jrs.8.084994](https://doi.org/10.1117/1.Jrs.8.084994), 2014.

1069  
1070 Thompson, C. R., Wofsy, S. C., Prather, M. J., Newman, P. A., Hanisco, T. F., Ryerson, T. B., Fahey, D. W.,  
1071 Apel, E. C., Brock, C. A., Brune, W. H., Froyd, K., Katich, J. M., Nicely, J. M., Peischl, J., Ray, E., Veres, P. R.,  
1072 Wang, S., Allen, H. M., Asher, E., Bian, H., Blake, D., Bourgeois, I., Budney, J., Bui, T. P., Butler, A.,  
1073 Campuzano-Jost, P., Chang, C., Chin, M., Commane, R., Correa, G., Crouse, J. D., Daube, B., Dibb, J. E.,  
1074 DiGangi, J. P., Diskin, G. S., Dollner, M., Elkins, J. W., Fiore, A. M., Flynn, C. M., Guo, H., Hall, S. R.,  
1075 Hannun, R. A., Hills, A., Hints, E. J., Hodzic, A., Hornbrook, R. S., Huey, L. G., Jimenez, J. L., Keeling, R. F.,  
1076 Kim, M. J., Kupc, A., Lacey, F., Lait, L. R., Lamarque, J.-F., Liu, J., McKain, K., Meinardi, S., Miller, D. O.,  
1077 Montzka, S. A., Moore, F. L., Morgan, E. J., Murphy, D. M., Murray, L. T., Nault, B. A., Neuman, J. A.,  
1078 Nguyen, L., Gonzalez, Y., Rollins, A., Rosenlof, K., Sargent, M., Schill, G., Schwarz, J. P., Clair, J. M. S.,  
1079 Steenrod, S. D., Stephens, B. B., Strahan, S. E., Strode, S. A., Sweeney, C., Thames, A. B., Ullmann, K.,  
1080 Wagner, N., Weber, R., Weinzierl, B., Wennberg, P. O., Williamson, C. J., Wolfe, G. M., and Zeng, L.: The  
1081 NASA Atmospheric Tomography (ATom) Mission: Imaging the Chemistry of the Global Atmosphere,  
*Bulletin of the American Meteorological Society*, 103, E761-E790, [10.1175/BAMS-D-20-0315.1](https://doi.org/10.1175/BAMS-D-20-0315.1), 2022.

1082  
1083 Turner, A. J., Frankenberg, C., Wennberg, P. O., and Jacob, D. J.: Ambiguity in the causes for decadal  
1084 trends in atmospheric methane and hydroxyl, *Proceedings of the National Academy of Sciences*, 114,  
5367, [10.1073/pnas.1616020114](https://doi.org/10.1073/pnas.1616020114), 2017.

1085  
1086 Turner, A. J., Fung, I., Naik, V., Horowitz, L. W., and Cohen, R. C.: Modulation of hydroxyl variability by  
1087 ENSO in the absence of external forcing, *Proc Natl Acad Sci U S A*, 115, 8931-8936,  
[10.1073/pnas.1807532115](https://doi.org/10.1073/pnas.1807532115), 2018.

1088  
1089 van Geffen, J., Boersma, K. F., Eskes, H., Sneep, M., ter Linden, M., Zara, M., and Veefkind, J. P.: S5P  
1090 TROPOMI NO<sub>2</sub> slant column retrieval: method, stability, uncertainties and comparisons with OMI,  
*Atmos. Meas. Tech.*, 13, 1315-1335, [10.5194/amt-13-1315-2020](https://doi.org/10.5194/amt-13-1315-2020), 2020.

1091  
1092 Veefkind, J. P., Aben, I., McMullan, K., Förster, H., de Vries, J., Otter, G., Claas, J., Eskes, H. J., de Haan, J.  
1093 F., Kleipool, Q., van Weele, M., Hasekamp, O., Hoogeveen, R., Landgraf, J., Snel, R., Tol, P., Ingmann, P.,  
1094 Voors, R., Kruizinga, B., Vink, R., Visser, H., and Levelt, P. F.: TROPOMI on the ESA Sentinel-5 Precursor: A  
GMES mission for global observations of the atmospheric composition for climate, air quality and ozone

- 1095 layer applications, *Remote Sensing of Environment*, 120, 70-83,  
1096 <https://doi.org/10.1016/j.rse.2011.09.027>, 2012.
- 1097 Verhoelst, T., Compernelle, S., Pinardi, G., Lambert, J. C., Eskes, H. J., Eichmann, K. U., Fjæraa, A. M.,  
1098 Granville, J., Niemeijer, S., Cede, A., Tiefengraber, M., Hendrick, F., Pazmiño, A., Bais, A., Bazureau, A.,  
1099 Boersma, K. F., Bognar, K., Dehn, A., Donner, S., Elokhov, A., Gebetsberger, M., Goutail, F., Grutter de la  
1100 Mora, M., Gruzdev, A., Gratsea, M., Hansen, G. H., Irie, H., Jepsen, N., Kanaya, Y., Karagiozidis, D., Kivi,  
1101 R., Kreher, K., Levelt, P. F., Liu, C., Müller, M., Navarro Comas, M., Piters, A. J. M., Pommereau, J. P.,  
1102 Portafaix, T., Prados-Roman, C., Puertedura, O., Querel, R., Remmers, J., Richter, A., Rimmer, J., Rivera  
1103 Cárdenas, C., Saavedra de Miguel, L., Sinyakov, V. P., Stremme, W., Strong, K., Van Roozendaal, M.,  
1104 Veeffkind, J. P., Wagner, T., Wittrock, F., Yela González, M., and Zehner, C.: Ground-based validation of  
1105 the Copernicus Sentinel-5P TROPOMI NO<sub>2</sub> measurements with the NDACC ZSL-DOAS, MAX-DOAS and  
1106 Pandonia global networks, *Atmos. Meas. Tech.*, 14, 481-510, 10.5194/amt-14-481-2021, 2021.
- 1107 Voulgarakis, A., Naik, V., Lamarque, J. F., Shindell, D. T., Young, P. J., Prather, M. J., Wild, O., Field, R. D.,  
1108 Bergmann, D., Cameron-Smith, P., Cionni, I., Collins, W. J., Dalsøren, S. B., Doherty, R. M., Eyring, V.,  
1109 Faluvegi, G., Folberth, G. A., Horowitz, L. W., Josse, B., MacKenzie, I. A., Nagashima, T., Plummer, D. A.,  
1110 Righi, M., Rumbold, S. T., Stevenson, D. S., Strode, S. A., Sudo, K., Szopa, S., and Zeng, G.: Analysis of  
1111 present day and future OH and methane lifetime in the ACCMIP simulations, *Atmospheric Chemistry and  
1112 Physics*, 13, 2563-2587, 10.5194/acp-13-2563-2013, 2013.
- 1113 Wang, P., Piters, A., van Geffen, J., Tuinder, O., Stammes, P., and Kinne, S.: Shipborne MAX-DOAS  
1114 measurements for validation of TROPOMI NO<sub>2</sub> products, *Atmos. Meas. Tech.*, 13, 1413-1426,  
1115 10.5194/amt-13-1413-2020, 2020.
- 1116 Wells, K. C., Millet, D. B., Payne, V. H., Deventer, M. J., Bates, K. H., de Gouw, J. A., Graus, M., Warneke,  
1117 C., Wisthaler, A., and Fuentes, J. D.: Satellite isoprene retrievals constrain emissions and atmospheric  
1118 oxidation, *Nature*, 585, 225-233, 10.1038/s41586-020-2664-3, 2020.
- 1119 Wild, O., Voulgarakis, A., amp, apos, Connor, F., Lamarque, J.-F., Ryan, E. M., and Lee, L.: Global  
1120 sensitivity analysis of chemistry-climate model budgets of tropospheric ozone and OH: exploring model  
1121 diversity, *Atmospheric Chemistry and Physics*, 20, 4047-4058, 10.5194/acp-20-4047-2020, 2020.
- 1122 Wolfe, G. M., Nicely, J. M., St Clair, J. M., Hanisco, T. F., Liao, J., Oman, L. D., Brune, W. B., Miller, D.,  
1123 Thames, A., Gonzalez Abad, G., Ryerson, T. B., Thompson, C. R., Peischl, J., McCain, K., Sweeney, C.,  
1124 Wennberg, P. O., Kim, M., Crouse, J. D., Hall, S. R., Ullmann, K., Diskin, G., Bui, P., Chang, C., and Dean-  
1125 Day, J.: Mapping hydroxyl variability throughout the global remote troposphere via synthesis of airborne  
1126 and satellite formaldehyde observations, *Proc Natl Acad Sci U S A*, 116, 11171-11180,  
1127 10.1073/pnas.1821661116, 2019.
- 1128 Wolter, K., and Timlin, M. S.: El Niño/Southern Oscillation behaviour since 1871 as diagnosed in an  
1129 extended multivariate ENSO index (MEI.ext), *International Journal of Climatology*, 31, 1074-1087,  
1130 10.1002/joc.2336, 2011.
- 1131 Zhao, Y., Saunio, M., Bousquet, P., Lin, X., Berchet, A., Hegglin, M. I., Canadell, J. G., Jackson, R. B.,  
1132 Hauglustaine, D. A., Szopa, S., Stavert, A. R., Abraham, N. L., Archibald, A. T., Bekki, S., Deushi, M., Jöckel,  
1133 P., Josse, B., Kinnison, D., Kirner, O., Marécal, V., Connor, F. M., Plummer, D. A., Revell, L. E., Rozanov, E.,  
1134 Stenke, A., Strode, S., Tilmes, S., Dlugokencky, E. J., and Zheng, B.: Inter-model comparison of global

- 1135 hydroxyl radical (OH) distributions and their impact on atmospheric methane over the 2000-2016  
1136 period, *Atmospheric Chemistry and Physics*, 19, 13701-13723, 10.5194/acp-19-13701-2019, 2019.
- 1137 Zhu, L., Jacob, D. J., Kim, P. S., Fisher, J. A., Yu, K., Travis, K. R., Mickley, L. J., Yantosca, R. M., Sulprizio, M.  
1138 P., De Smedt, I., González Abad, G., Chance, K., Li, C., Ferrare, R., Fried, A., Hair, J. W., Hanisco, T. F.,  
1139 Richter, D., Jo Scarino, A., Walega, J., Weibring, P., and Wolfe, G. M.: Observing atmospheric  
1140 formaldehyde (HCHO) from space: validation and intercomparison of six retrievals from four satellites  
1141 (OMI, GOME2A, GOME2B, OMPS) with SEAC<sup>4</sup>RS aircraft observations over the southeast US,  
1142 *Atmospheric Chemistry and Physics*, 16, 13477-13490, 10.5194/acp-16-13477-2016, 2016.  
1143
- 1144 Zhu, Q., Laughner, J. L., and Cohen, R. C.: Estimate of OH trends over one decade in North American  
1145 cities, *Proc Natl Acad Sci U S A*, 119, e2117399119, <https://doi.org/10.1073/pnas.2117399119>, 2022a.
- 1146 Zhu, Q., Laughner, J. L., and Cohen, R. C.: Combining Machine Learning and Satellite Observations to  
1147 Predict Spatial and Temporal Variation of near Surface OH in North American Cities, *Environmental  
1148 Science & Technology*, 7362 - 7371, 10.1021/acs.est.1c05636, 2022b.  
1149